



A global record of single-layered ice cloud properties and associated radiative heating rate profiles from an A-Train perspective

Erica K. Dolinar^{1,6} · Xiquan Dong² · Baike Xi² · Jonathan H. Jiang³ · Norman G. Loeb⁴ · James R. Campbell⁵ · Hui Su³

Received: 27 September 2018 / Accepted: 11 February 2019 / Published online: 15 March 2019
© Springer-Verlag GmbH Germany, part of Springer Nature 2019

Abstract

A record of global single-layered ice cloud properties has been generated using the CloudSat and CALIPSO Ice Cloud Property Product (2C-ICE) during the period 2007–2010. These ice cloud properties are used as inputs for the NASA Langley modified Fu–Liou radiative transfer model to calculate cloud radiative heating rate profiles and are compared with the NASA CERES observed top-of-atmosphere fluxes. The radiative heating rate profiles calculated in the CloudSat/CALIPSO 2B-FLXHR-LIDAR and CCCM_CC products are also examined to assess consistency and uncertainty of their properties using independent methods. Based on the methods and definitions used herein, single-layered ice clouds have a global occurrence frequency of ~18%, with most of them occurring in the tropics above 12 km. Zonal mean cloud radiative heating rate profiles from the three datasets are similar in their patterns of SW warming and LW cooling with small differences in magnitude; nevertheless, all three datasets show that the strongest net heating ($> +1.0 \text{ K day}^{-1}$) occurs in the tropics (latitude $< 30^\circ$) near the cloud-base while cooling occurs at higher latitudes ($> \sim 50^\circ$). Differences in radiative heating rates are also assessed based on composites of the 2C-ICE ice water path (IWP) and total column water vapor (TCWV) mixing ratio to facilitate model evaluation and guide ice cloud parameterization improvement. Positive net cloud radiative heating rates are maximized in the upper troposphere for large IWPs and large TCWV, with an uncertainty of 10–25% in the magnitude and vertical structure of this heating.

Keywords Single-layered ice cloud properties · Radiative heating rate profiles · Satellite remote sensing

1 Introduction

The Earth radiation budget is a focal point of the changing climate system (i.e., Wielicki et al. 1996; Loeb et al. 2007; Kato et al. 2015; L’Ecuyer et al. 2015). With clouds being a primary modulator of the radiation budget (Ramanathan

et al. 1989; Hartmann et al. 1992; Randall et al. 2007), correctly observing and modeling their properties have become an extensive undertaking over the past several decades. The redistribution of radiation (i.e., energy) in the atmosphere caused by clouds has important implications for large-scale circulation patterns and the hydrological cycle (Larson and Hartmann 2003; Wild et al. 2004).

Ice clouds play a unique role in the balance of radiation in the atmosphere. In general, the magnitude of warming or cooling that clouds produce is determined by their microphysical properties, optical depth, vertical distribution and horizontal extent, prevalence during the day or night, latitude, and the underlying surface characteristics (Stephens and Webster 1981; Fu and Liou 1993; Campbell et al. 2016). Each of these impact the amount of in-cloud absorption and emission of longwave (LW, wavelength $\lambda = 5\text{--}100 \mu\text{m}$) radiation and the absorption and reflection/scattering of shortwave (SW, wavelength $\lambda = 0\text{--}5 \mu\text{m}$) radiation. Since ice clouds exist in a variety of conditions, and form through several different pathways (Sassen et al. 2008; Cziczo et al.

✉ Xiquan Dong
xdong@email.arizona.edu

¹ Department of Atmospheric Sciences, University of North Dakota, Grand Forks, ND, USA

² Department of Hydrology and Atmospheric Sciences, University of Arizona, 1133 E. James Rogers Way, P.O. Box 210011, Tucson, AZ 85721-4652, USA

³ Jet Propulsion Laboratory, Pasadena, CA, USA

⁴ NASA Langley Research Center, Hampton, VA, USA

⁵ Naval Research Laboratory, Monterey, CA, USA

⁶ Present Address: American Society for Engineering Education, Washington, DC, USA

2013), and given that cirrus clouds themselves are the most common cloud type in the atmosphere (Mace et al. 2009; Stubenrauch et al. 2013), quantifying their radiative impacts is extremely important.

Active remote sensing platforms, such as IceSat-1, CloudSat, and the Cloud-Aerosol Lidar and Infrared Pathfinder Satellite Observations (CALIPSO), began measuring the vertical structure of clouds from space in the early to mid-2000's. Since then, modeling of radiative flux profiles has become more prolific on the global scale (e.g., L'Ecuyer et al. 2008, Su et al. 2009). Specifically, with the inclusion of Cloud Aerosol Lidar with Orthogonal Polarizationn (CALIOP) on board CALIPSO, optically-thin ice clouds (optical depth, $\tau < 0.3$; Sassen and Cho 1992), which exert a measurable impact on the radiation budget, are being monitored with better accuracy (Chiriaco et al. 2007; Minnis et al. 2008; Kox et al. 2014).

CloudSat and CALISPO are members of the A-Train satellite constellation (L'Ecuyer and Jiang 2010) orbiting the Earth ~15 times a day on a sun-synchronous orbit at ~700 km above the surface. Kato et al. (2011) describe the impacts that the CloudSat cloud profiling radar (CPR) and CALIOP data have on irradiance computations. For 1 year of instantaneous TOA fluxes, their computed results match better with Clouds and Earth's Radiant Energy System (CERES)-derived fluxes to within 0.5 and 2.6 W m⁻² for SW and LW, respectively, compared with calculations using derived cloud properties based on Moderate Resolution Imaging Spectroradiometer (MODIS) measurements. Similarly, at the surface, their calculated global mean instantaneous downward SW and LW fluxes change by -8.6 and +3.4 W m⁻², respectively, due to larger cloud fractions and lower cloud-base heights compred with MODIS.

A particular facet of cloud-radiative balance, particularly within numerical climate modeling simulations and daily weather forecasting, relates directly to the impact of ice-phase clouds (including both cirrus and glaciated cloud elements). Most global simulations treat ice as a single mode, allowing only one ice parameterization (e.g., cirrus cloud nucleation and the glaciation of liquid water clouds) to operate at any one time in a grid-box. Correctly resolving the radiative impacts of single-layered ice clouds from satellite-resolved cloud microphysical properties is a compulsory means for conducting requisite model evaluation. For instance, the evolution of deep convective and large-scale cloud systems in GCMs partially relies on the detrainment of cloud ice (Del Genio et al. 2012; Elsaesser et al. 2017), which as an extension can be regarded as a driver of the radiative heating of the clouds (or vice versa). Furthermore, profiles of cloud radiative heating can act to modify the stability of the environment and affect vertical motion (Del Genio et al. 2012). Vertical radiative heating rates can therefore be used to diagnose errors in simulated cloud fields

in GCMs and perhaps improve detrainment, as well as the occurrence and development of ice clouds.

Jiang et al. (2012) reports some improvements of simulated ice clouds in the Coupled Model Intercomparison Project Phase 5 (CMIP5) compared with their earlier versions in CMIP3. Although the mean bias and spread of ice water content (IWC) were reduced in the CMIP5 model versions, some notable discrepancies in the simulated ice clouds were found. Considerable spread and bias in the simulated upper tropospheric (~215 and 100 hPa) IWC and water vapor in the tropics (30°N–30°S) were found when compared with Microwave Limb Sounder (MLS) and CloudSat retrievals (Jiang et al. 2010, 2012; Li et al. 2012). Additionally, the simulated diurnal variation of partial ice water path (IWP) over the tropical upper troposphere shows bias in the mean state, amplitude, and phase compared with the Superconducting Submillimeter Limb Emission Sounder (SMILES) on board the International Space Station (ISS), especially over ocean, suggesting a poor understanding of their development (Jiang et al. 2015).

Single-layered ice clouds are sampled for this study due to the relative simplicity in isolating their effects on the Earth radiation budget and relatively straight-forward intercomparison with corresponding model simulations. The interaction of radiation with multi-layered clouds and precipitation is a more complex problem (Li et al. 2011). Cloud overlap assumptions used in current modeling frameworks are oftentimes oversimplified or incorrectly represented and can lead to large biases in simulated radiation fields, especially for highly complex cloud systems such as deep convection (Liang and Wang 1997; Barker et al. 1999; Hogan and Illingworth 2000; Zhang et al. 2013). Moreover, singling out the radiative impact of ice clouds when they are close in proximity to falling hydrometeors further complicates the matter. While there is certainly a need for better resolving the radiative effects of multi-layer clouds, determining the radiative effects of single-layered ice clouds is the first step towards a comprehensive quantification of the radiative effects of clouds, which is important for improving global model simulations.

The current study reports on the consistency of modeled TOA and surface SW/LW radiative fluxes and the radiative heating rate (Q_r) profiles of single-layered ice clouds from an assortment of independently-developed datasets. We could justify sampling only the ice cloud radiative properties derived and reported in 2B-FLXHR-LIDAR (Henderson et al. 2013) or CCCM (Kato et al. 2011) for this study. However, in calculating these radiative properties independently, we are adding a unique dataset to the estimates of the radiative effects of single-layered ice clouds. L'Ecuyer et al. (2015) remarks on the advantages of multiple radiative flux datasets for better uncertainty quantification. By analyzing an assortment of datasets developed based on a

variety of spatial resolutions, inputs from specific sensors, different radiative transfer models, and different diurnal sampling offers a reasonable approximation of the “aggregate effects of structural errors” in each product (L’Ecuyer et al. 2015). Bearing this in mind, these new calculations can also indicate the impact of cloud retrievals on estimating cloud radiative properties. This is particularly crucial since the observed vertical structure of radiative heating by ice clouds is not fully constrained (Cesana et al. 2017).

Therefore, the purpose of this study is to provide a broad perspective of the impact that single-layered ice clouds have on the global Earth radiation budget through consideration of their heating rate profiles. Our goal is to generate a global record of single-layered ice cloud physical and radiative properties (Sect. 3). In addition, we composite their heating rate profiles based on cloud and environmental properties typically simulated by GCMs (Sect. 4). By relating the computed heating rate profiles to radiatively-dependent components of the clouds or background environment, we facilitate a treatment of bulk ice cloud properties which can be used in future model development and evaluation efforts.

2 Data, methods, and tools

One major caveat to the methods used herein is the aggregation of several ice types (e.g., glaciated ice versus cirrus) as one entity. We assume that the cloud properties from CloudSat and CALIPSO are a one-size fits all approximation in terms of their optical properties. Of course, different types of ice clouds should be handled differently when parameterized in cloud retrievals and in radiative transfer modeling (Yi et al. 2017a, b). This includes ice crystal shape, particle size distribution (PSD), and resulting changes in scattering/absorption properties.

Yi et al. (2017a, b) describe the change in global ice cloud TOA cloud radiative effects (CREs) based on cloud mask differences and differences in parameterized ice cloud property retrievals in MODIS collection 5.1 (C51) and 6 (C6) and of the parameterized ice in the radiative transfer model (RTM). They develop new ice cloud optical parameterizations to remain consistent with the two MODIS cloud parameterizations. C6 yields a weaker TOA SW CRE (i.e., less cooling) compared with C51 due to the larger retrieved cloud effective radii (by $\sim 6.7 \mu\text{m}$) and optical depth (by $\sim 25\%$; Yi et al. 2017b). While little change occurs in the LW CRE between C51 and C6, the net ice CRE in C6 changes sign due to impacts in the SW. Yi et al. (2017a, b) also perform a sensitivity study focusing on the differences in TOA CREs when inconsistent parameterization schemes are used for cloud retrievals and in the RTM. The TOA SW and LW ice CREs change by -15.83 and 0.06 W m^{-2} , respectively, in C6 when the ice particle habits

are modified. Notwithstanding, Loeb et al. (2018) explain that the retrieved cloud optical properties (i.e., optical depth or effective radius) are actually more sensitive to the ice particle model, as opposed to the ice particle model used for radiative flux calculations.

2.1 2C-ICE ice cloud properties

With the combination of the CloudSat CPR (operating at 94 GHz) (Stephens et al. 2002) and the CALIOP (532 and 1064 nm; Winker et al. 2009) coincident measurements of vertically-resolved aerosols, subvisible and thin cirrus, and optically-thick clouds are attainable on the global scale (Deng et al. 2010, 2015). The CPR measures back-scattered power every 240 m vertically on a footprint of $1.4 \text{ km} \times 1.8 \text{ km}$ (across \times along track) with a sensitivity of -30 dBZ_e (Deng et al. 2010). CALIOP, on the other hand, measures the attenuated backscatter every 30–70 m vertically on a footprint of $0.075 \text{ km} \times 0.3\text{--}1.0 \text{ km}$ (across \times along track) (Deng et al. 2010). For this study, the satellite-retrieved ice cloud physical properties (i.e., IWC and R_e) data come from the merged CloudSat and CALIPSO Ice cloud property product (2C-ICE P1_R04; Deng et al. 2010, 2015). Ice cloud boundaries are defined from the 2B-GEO-PROF-LIDAR (Mace et al. 2009) and 2B-CLDCLASS-LIDAR products (Sassen et al. 2008).

The 2C-ICE algorithm defines three separate regions within a profile: the lidar-only, radar-only, and the lidar-radar overlap regions. These zones are defined based upon sensor sensitivity/attenuation, which allows for respective data processing methodologies in each region (e.g., parameterizations or measurement error assignment; Deng et al. 2010). The largest sources of uncertainty in 2C-ICE result from the retrieval algorithm assumptions related to ice particle size distributions (PSD; a modified gamma distribution in this algorithm; Deng et al. 2010) and particle habit oversimplification, multiple scattering assumptions related to the lidar signal, and the radar reflectivity parameterizations in the lidar-only region (Deng et al. 2015). Errors in the assumptions based on multiple scattering can lead to an uncertainty of $\sim 15\%$ in optical depth and $\sim 30\%$ or more in IWC. The cloud ice particle effective radii (R_e), available in the 2C-ICE product, were computed from the best estimate of PSD. Although estimates of cloud-top R_e are available on the global scale (e.g., Kahn et al. 2018), no direct measurements of R_e profiles are currently available on the global scale (Jiang et al. 2017), and, therefore, a large uncertainty may exist in the R_e used for the radiative transfer modeling.

2.2 Radiative transfer model

One-dimensional radiative transfer modeling of broadband fluxes is performed. The FLux model for CERES with

k-distribution and correlated-k for Radiation (FLCKKR) radiative transfer model (with a two-stream approximation) is used, which is an earlier version of the NASA Langley modified Fu–Liou radiative transfer model (Fu and Liou 1993; Fu et al. 1997; Kato et al. 1999). The LW and SW radiative fluxes are calculated with several options; a δ -four- or δ -two/four-stream solver and a δ -two, δ -four, or gamma weighted δ -two-stream solver, respectively (Kato et al. 2005). This study utilizes the two-stream solver for SW calculations while the two/four-stream solver is used for the LW. For the SW and LW fluxes, a total of 18 and 14 bands are computed, respectively, which are sensitive to specific gaseous species. A total of 25 different aerosol types are featured in this model and are characterized by their own spectral normalized extinction, scattering, and absorption properties.

Single-scattering ice particle properties (e.g., phase function, single-scattering albedo, and extinction coefficient) are parameterized through exploitation of in-situ aircraft data and based on the assumptions that ice crystals are randomly oriented and ice crystal absorption is small (Fu and Liou 1993). The δ -four-stream model used for calculating solar and infrared radiative flux transfer in a single homogeneous or nonhomogeneous layer can provide radiative fluxes with an accuracy of 5%.

2.3 Radiative transfer input

In addition to the vertically-discretized ice cloud properties from 2C-ICE, several other radiatively dependent properties are ingested to the radiative transfer model (RTM) once the subset of single-layered ice clouds is established. Meteorological profiles (i.e., temperature, water vapor, and ozone) come from the European Centre for Medium-range Weather Forecasting (ECMWF) auxiliary product, which

are interpolated to the CloudSat radar bins from the surface to ~ 25 hPa. For this study, the profiles are extended to ~ 0.01 hPa by collocating consistent retrievals from the Microwave Limb Sounder (MLS; version 4.2). The uncertainties in temperature, water vapor, and ozone from MLS are 1 K, 10–50%, and 5–10%, respectively (Read et al. 2007; Froidevaux et al. 2008; Schwartz et al. 2008). Surface and aerosol properties come from the data available in the CALIPSO CloudSat CERES and MODIS (CCCM) Edition B1 product (Kato et al. 2014). Table 1 lists the input parameters and data sources used in applying the RTM in this study and for the other products investigated. All CloudSat and MLS pixel data are collocated to the CCCM pixels since the CCCM pixels have the coarsest resolution of 20 km. In order to account for the variability in insolation throughout the year, a correction to the total solar irradiance is also applied based on the Sun-Earth distance. For simplicity, the fluxes calculated in this study will be referred to as D18.

2.4 Sampling method and occurrence frequency

Single-layered ice cloud pixels are first subset based on the 2C-ICE IWC and 2B-CWC-RVOD (Austin and Stephens 2001; Austin et al. 2009) liquid water content (LWC) profiles. The IWC/ R_e profiles are retained assuming they are vertically continuous with no liquid clouds (i.e., LWC) existing in the column. Additionally, profiles with detectable precipitation, as per the 2C-PRECIP-COLUMN (Haynes et al. 2009) product, are also removed. Figure 1 displays an example of the single-layered ice cloud detection using this definition. Notice that 2C-ICE provides an IWC retrieval for the mixed-phase portion of the cloud (i.e., Fig. 1a, b at 58° – 64° S and 1–5 km; $IWC > \sim 0.3 \text{ g m}^{-3}$), but it is effectively removed from the subset in this study based on consideration of the 2B-CWC-RVOD LWC (Fig. 1c) profile (grey

Table 1 Descriptions of the input parameters used to produce the calculated fluxes investigated in this study

	D18	2B-FLXHR-LIDAR ^a	CCCM_CC ^b
RTM	FLCKKR	BugsRad	FLCKKR
IWC/Re	2C-ICE	2B-CWC-RO, 2B-TAU, CAL_LID_L2_05kmCLay	CloudSat CPR (Revision 4), CALIPSO (V3), MODIS
Meteorology (T, H ₂ O, O ₃)	ECMWF-AUX and MLS	ECMWF-AUX ^c	GEOS-5
Surface Albedo	CERES/MODIS	IGBP	MODIS
AOD	CALIPSO or MERRA-2 ^d	CALIPSO Level 2 vertical feature mask	CALIPSO, MOD04, MATCH
Aerosol type	MATCH	CALIPSO Level 2 vertical feature mask	MATCH
Skin temperature	ECMWF-AUX	ECMWF-AUX	GEOS-4/-5

^aIGBP International Geosphere-Biosphere Programme, ^bMATCH Model for Atmospheric Transport and Chemistry

^cProfiles extend only to 25 km

^dColumn integrated AOD at one wavelength

^aHenderson et al. (2013)

^bKato et al. (2011)

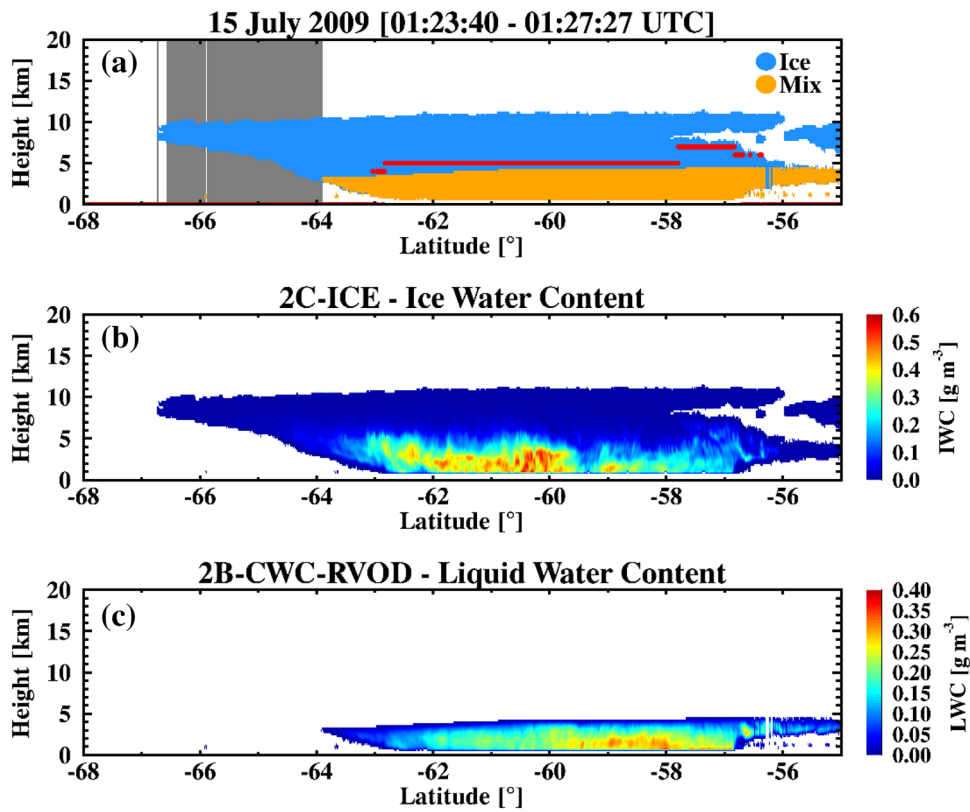


Fig. 1 An example of the detection algorithm for single-layered ice clouds on 15 July 2009 over the Southern Ocean. **a** Orange areas correspond to layers of the cloud containing a mix of liquid (from 2B-CWC-RVOD) and ice (from 2C-ICE) while the blue area is ice only. The horizontal red lines correspond to profiles when precipitation is detected by the Cloud Profiling Radar (CPR; 2C-PRECIP-COLUMN). Values indicate what type of precipitation is detected and the certainty of detection (rain: 1—possible, 2—probable, 3—certain;

snow: 4—possible, 5—certain; mixed: 6—possible, 7—certain). For this cloud system both snow and mixed precipitation were detected (refer to the legend in **a**). The grey section represents where the algorithm defines single-layered ice clouds used in this study. **b** The 2C-ICE IWC and **c** 2B-CWC-RVOD LWC (g m^{-3}) for the cloud of interest is contoured to showcase that 2C-ICE retrieves not only ice clouds but also the ice of mixed phase clouds

shaded region from $\sim 64^\circ$ to 66.5°S in Fig. 1a highlights the single-layered ice cloud based on this definition). The precipitation detection by 2C-PRECIP-COLUMN also indicates that snow or mixed precipitation (flagged as 4–7, the red horizontal lines in Fig. 1a) is present within the cloud.

Based on these simple criteria, the global occurrence frequency of single-layered ice clouds is generated and shown in Fig. 2. Single-layered ice clouds occur most frequently ($> 25\%$) in the tropical warm pool of the western Pacific, Indonesia, and central Africa, and northern South America. These clouds are relatively infrequent in the Southern Ocean and the oceanic western continental coasts due to the larger frequency of marine boundary layer clouds formed in the descending branch of the Hadley Cell. In addition to global horizontal distribution, their vertical occurrence frequency distributions are illustrated in Fig. 2b, where single-layered ice clouds occur more than $\sim 10\%$ of the time in the tropics at an altitude of 12–16 km. Antarctica also experiences these clouds with considerable frequency near 5 km; polar

stratospheric clouds (PSCs) contribute $\sim 15\%$ to this amount. The global occurrence frequency is roughly 18% in this study. The occurrence is slightly larger during the nighttime, most notably over Antarctica between 5 and 10 km and in the tropics above ~ 15 km (not shown).

2.5 Additional radiative flux datasets

Diagnosing the differences in calculated irradiance profiles from multiple independent data sources provides an estimate of their variance. Comparing the calculated irradiances to observed ones provides an assessment of consistency. Since directly-measured irradiance profiles are not available at this time, it is difficult to constrain their modeled values. Therefore, we are limited to comparing the calculated TOA fluxes with instantaneous CERES-derived irradiances. Observed surface irradiances can also be used to constrain the calculated surface fluxes, but this is limited to infrequent overpasses and corresponding sparse coverage of ground sites.

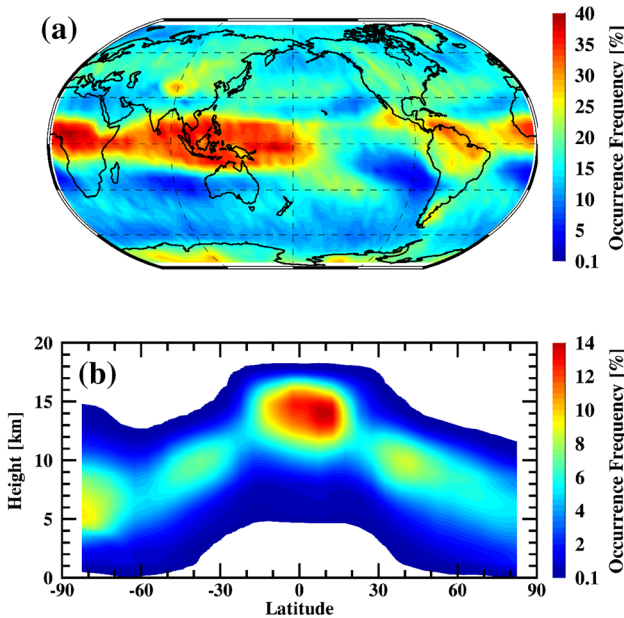


Fig. 2 The 4-year (2007–2010) global **a** horizontal and **b** vertical occurrence frequency (%) distributions of single-layered ice clouds identified by 2C-ICE. Frequencies are on a $5^\circ \times 5^\circ$ horizontal and 250 m vertical grid. Occurrence frequency (%) = $(N_{\text{ice_cld}}/N_{\text{total}}) \times 100$

The instantaneous nadir-view TOA irradiances derived from CERES are from the single scanner footprint (SSF) Edition3-Beta2 product reported in CCCM. TOA fluxes are obtained by applying empirical angular distribution models to CERES-observed SW and LW radiances (Loeb et al. 2005).

CCCM offers calculated irradiance profiles from the surface to the TOA (138 levels) with MODIS-derived cloud properties from an enhanced CERES algorithm, integrated with measured cloud information from and along the CloudSat and CALIPSO ground track (Kato et al. 2011). For the subset of single-layered ice clouds sampled in this study, 31% of the pixels are contributed by observations from a combination of CloudSat, CALIPSO, and MODIS, while $\sim 26\%$ (~ 17 or 15%) are from CALIPSO (MODIS and CALIPSO or CloudSat and CALIPSO) only. The CCCM-calculated irradiances from this dataset will be henceforth referred to as CCCM_CC. Kato et al. (2010, 2011) provide more extensive assessments of how CloudSat, CALIPSO, and MODIS cloud scenes are integrated to produce a coherent cloud signal and how the irradiance profiles are calculated in CCCM_CC. The RTM used to calculate the irradiance profiles in CCCM_CC is the same one used for this study. Therefore, we can conclude that the differences in irradiance estimates between CCCM_CC and those generated for this study (i.e., D18) are due to the differences in input data (e.g., cloud and aerosol properties and background meteorology). Moreover, differences related to our definition and

identification of non-precipitation single-layer ice clouds can contribute to these differences.

In addition to CCCM_CC, the radiative flux profiles from the 2B-FLXHR-LIDAR (P2_R04; L'Ecuyer et al. 2008; Henderson et al. 2013) product are also examined for single-layered ice clouds. The 2B-FLXHR-LIDAR product provides estimates of broadband radiative flux profiles from the surface to the lower stratosphere at the observed CloudSat CPR range gates (125 levels). Liquid and ice cloud properties and precipitation are derived from observed CPR, CALIOP, and MODIS properties (although liquid and precipitating clouds have been removed for this study). Henderson et al. (2013) provided a detailed description of how liquid and ice clouds are represented in 2B-FLXHR-LIDAR, including sensor limitations and how these limitations are minimized. Table 1 lists the various input parameters and their source products for the three calculated flux datasets examined in this study.

3 Single-layered ice cloud physical properties

3.1 Ice water content/path (IWC/P) and effective radius (R_e)

The vertical distributions of IWC and R_e effectively determine how solar and infrared radiation interacts with a cloud via scattering and absorption. Before analyzing the radiative properties of single-layered ice clouds, their global micro- and macrophysical properties should first be examined and understood. Since this study bears no restriction on the optical thickness or height of single-layered ice clouds, these properties characterize a variety of ice cloud types (e.g., cirrus, cirrostratus, thick anvil, etc.).

Figure 3a–c depict the global mean averages of 2C-ICE IWP, and vertical profiles of mean IWC and R_e as a function of latitude, respectively. The largest grid box ($5^\circ \times 5^\circ$) average IWPs ($> 65 \text{ g m}^{-2}$) occur along mid-latitude storm tracks in the northern and southern Pacific and Atlantic Oceans. The smallest IWPs ($< 15 \text{ g m}^{-2}$) are found in regions where the occurrence frequency is small, such as the western coasts of Africa, South America, and Australia. The IWP is also quite small in Antarctica despite the relatively large occurrence frequency there (i.e., Fig. 2). The single-layered ice clouds observed in Antarctica are optically thin, enhanced by the contribution of polar stratospheric clouds (PSCs). The highest IWCs ($> \sim 45 \text{ mg m}^{-3}$) in the mid-latitudes and tropics occur at altitudes of ~ 4 – 8 km. R_e follows a similar pattern to IWC with the largest particles ($> 50 \mu\text{m}$) occurring in the tropics and mid-latitudes at an altitude of ~ 3 – 8 km.

The IWP/C probability distribution function (PDF) and cumulative distribution function (CDF) are illustrated in

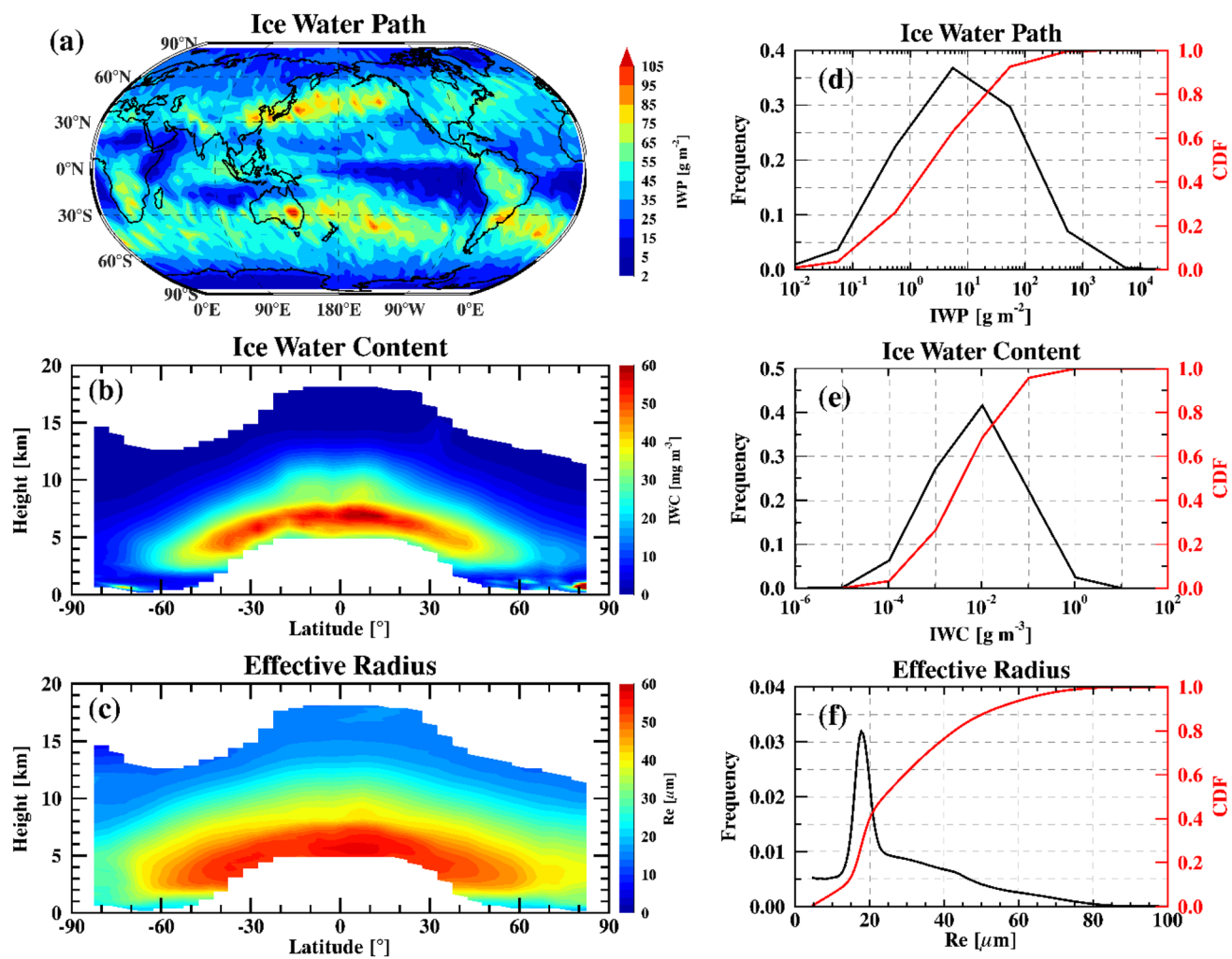


Fig. 3 **a** The annual mean global distribution of ice water path (IWP, g m^{-2}) and **b** the latitude-height cross-sections of **b** ice water content (IWC, mg m^{-3}) and **c** effective radius (R_e , μm) for single-layered ice clouds. Vertical cross-sections contain only cloudy portions of the profile (i.e., $\text{IWC} > 0.0 \text{ g m}^{-3}$ and $R_e > 0.0 \mu\text{m}$) and when the occurrence frequency is greater than 0.1% (see Fig. 2). The right column shows the frequency and CDFs of pixel-level **d** IWP, **e** IWC, and **f** R_e values. IWC and R_e values are retained only when the $R_e > 4.5 \mu\text{m}$, which is the lower limit for calculating radiative fluxes for ice clouds in this study

rence frequency is greater than 0.1% (see Fig. 2). The right column shows the frequency and CDFs of pixel-level **d** IWP, **e** IWC, and **f** R_e values. IWC and R_e values are retained only when the $R_e > 4.5 \mu\text{m}$, which is the lower limit for calculating radiative fluxes for ice clouds in this study

Fig. 3d, e, based on all available pixel-level ice cloud property retrievals from 2C-ICE. Figure 3d shows that most IWP retrievals fall within a range of $0.1\text{--}400 \text{ gm}^{-2}$ with a mode of 5 g m^{-2} . Approximately 70% of the retrievals have IWPs (IWCs) below 10 g m^{-2} (10^{-2} g m^{-3}) and only $\sim 10\%$ (5%) are above 100 g m^{-2} (10^{-1} g m^{-3}). Therefore, a significant portion of the single-layered ice clouds in this study contain relatively small amounts of ice. The mode of ice cloud effective radius is $\sim 18 \mu\text{m}$, and only $\sim 10\%$ of the samples are greater than $60 \mu\text{m}$.

3.2 Single-layered ice cloud-top and -base heights and temperatures

Figure 4 features the monthly zonal means of cloud-top and cloud-base heights (a, b) and temperatures (d, e) for

single-layered ice clouds derived from the 2C-ICE cloud properties and ECMWF-AUX. The highest and coldest cloud-top heights ($> 14 \text{ km}$) and temperatures ($< 205 \text{ K}$) occur in the tropics during northern hemisphere winter months (DJF) (Fig. 4a, d). The ice cloud-top temperatures over the tropics are just as cold as in the Antarctic during local winter, which is consistent with Campbell et al. (2008) and the influence of PSCs. Our results do capture a corresponding increase in ice cloud-top height ($\sim 2.75 \text{ km}$) from local summer to winter months in Antarctica. Gridded monthly zonal mean ice cloud-base heights and temperatures can reach as low as $\sim 3.25 \text{ km}$ and as high as 253 K .

The ice cloud-top and -base heights over the mid-latitudes appear to have a stronger seasonal dependence compared with the cloud temperatures. For example, the

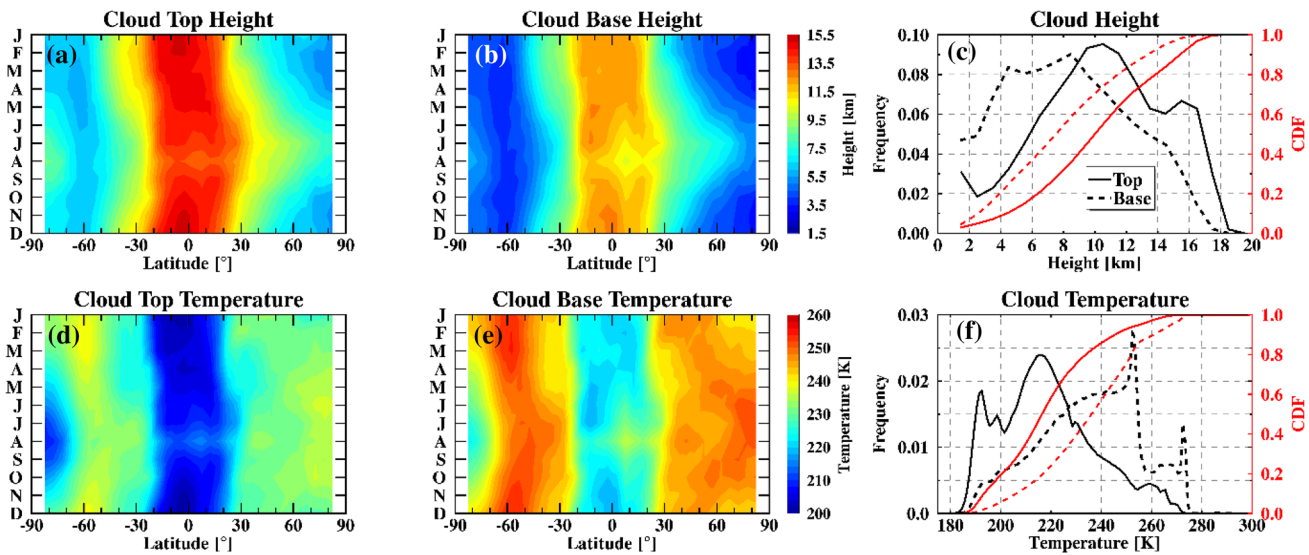


Fig. 4 Contoured are the gridded ($5^\circ \times 5^\circ$) monthly zonal means of cloud-top (left) and cloud-base (middle) heights (km, top) and temperature (K, bottom) for single-layered ice clouds. The right column (c, f) shows the frequency (black) and cumulative frequencies (red) of

cloud-top (solid) and cloud-base (dashed) heights and temperatures. Height bins are 1 km wide from 1 to 20 km and the temperature bins are 1 K wide from 175 to 299 K

ice cloud-top and -base heights are higher in the northern hemisphere summer months and extend further into the higher latitudes (Fig. 4a, b). However, this evolution is not apparent in the cloud temperatures (Fig. 4d, e). On average, the tropopause height decreases with latitude toward the poles but shifts north/southward with season (i.e., the tropopause height is higher/colder during local summer over the northern mid-latitudes compared to the winter), so it is easy to understand why we do not see a similar change in temperatures (Nazaryan et al. 2008).

PDFs of the cloud-top and -base heights and temperatures reveal a bi-modal distribution (Fig. 4c, f) for pixel-level ice cloud retrievals. The primary mode of cloud-top height (temperature) is at ~ 11 km likely represents mid-latitude ice clouds (~ 215 K) while the secondary mode at 15 km corresponds to tropical convective outflow or tropical tropopause layer (TTL) ice clouds (~ 190 Virts and Wallace 2010). Campbell et al. (2016) reported the PDFs of daytime single-layered cirrus cloud-top heights observed by the micropulse lidar (MPL; 532 nm) at the mid-latitude Goddard Space Flight Center in Greenbelt, Maryland for one year of data. Based on their analysis, cloud-top heights range from 6 to 16 km (for cloud-top temperature ≤ -37 °C and cloud depth between 0 and 5 km) with a peak in the distribution at 11 km. Cloud-tops warmer than 273 K, the approximate upper thermal bound where homogeneous freezing of liquid water dominates and proxy cloud-top temperature threshold minimum distinguishing cirrus clouds from glaciated clouds in the absence of ancillary evidence aside from lidar

measurements (see Campbell et al. 2015), represent the impact of glaciated clouds within the bulk cloud sample.

4 Ice cloud radiative properties

Four years (2007–2010) of radiative flux profiles are calculated from the surface to the TOA for every 2C-ICE pixel collocated to CCCM using the input data introduced in Table 1. Before assessing the differences in heating rate profiles from the three calculated flux datasets listed above, we first evaluate the consistency of these calculated fluxes at the TOA and surface with the observed fluxes from CERES and the Atmospheric Radiation Measurement (ARM) Program, respectively. We focus on daytime only pixels (solar zenith angle, SZA, less than 90°) for this analysis. Global TOA fluxes are averaged to a $5^\circ \times 5^\circ$ grid.

4.1 TOA and surface radiative fluxes

Four years of instantaneous TOA-reflected SW and outgoing LW radiative fluxes for ice cloudy pixels are shown in Figs. 5 and 6, respectively. The CERES-derived and CCCM_CC calculated SW fluxes at the TOA are very similar in terms of their global means (241.52 and 242.20 W m^{-2} , respectively, with a RMSD of 12.18 W m^{-2} ; see Table 2) and geographic distribution. Compared with CERES, the calculated TOA reflected SW fluxes from 2B-FXHR-LIDAR and D18 are, on average, too small by 47.07 (19%) and 31.33 W m^{-2} (13%), respectively, with even larger RMSDs and relatively small

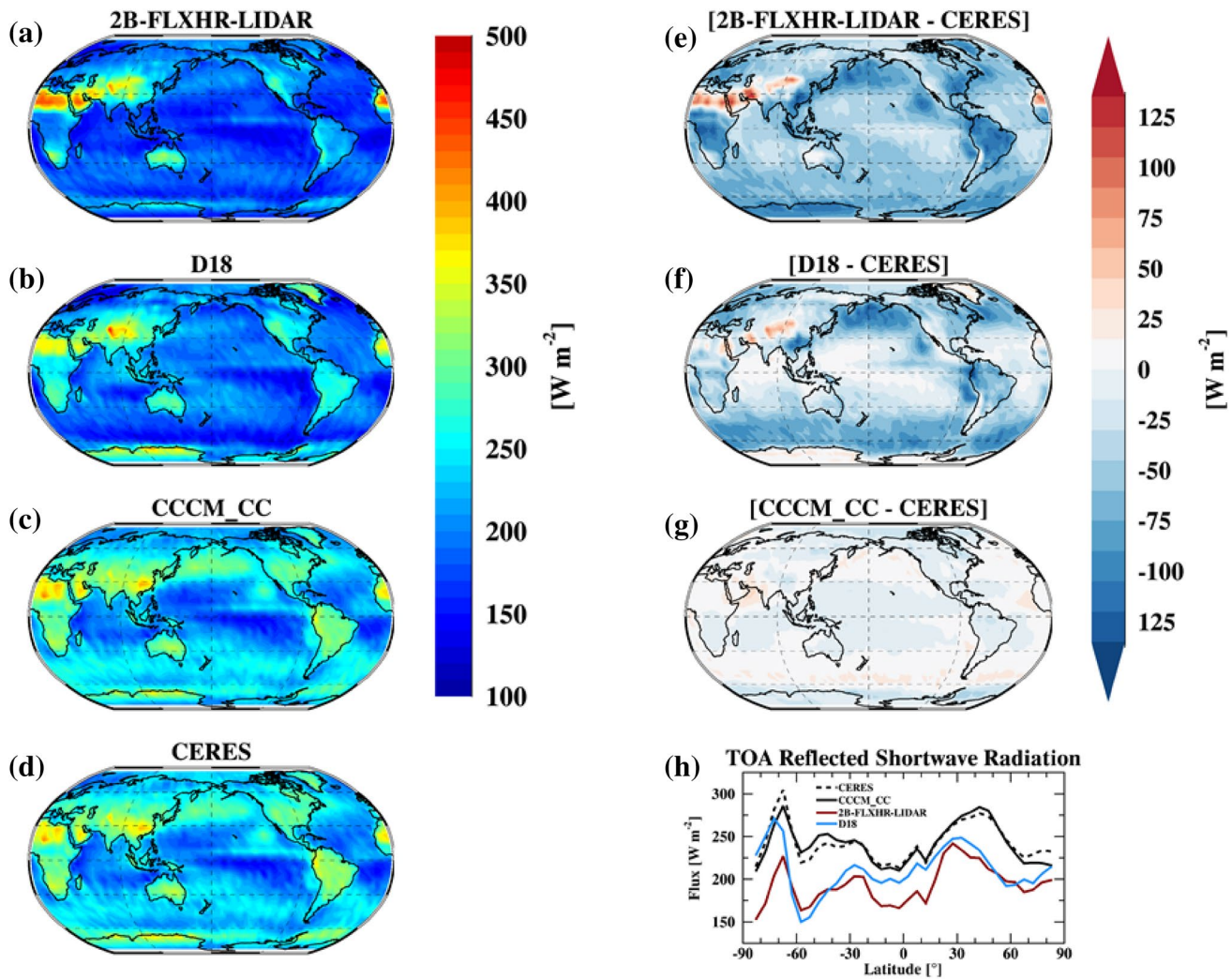


Fig. 5 Global maps of the TOA reflected SW fluxes and their differences (calculated minus CERES) for single-layered ice clouds during 2007–2010 for **a**, **e** 2B-FLXHR-LIDAR, **b**, **f** D18 (this study), **c**,

g CCCM_CC, and **d** CERES. **h** The zonal variations are presented with CERES in the black dashed line and CCCM_CC, 2B-FLXHR-LIDAR, and D18 in solid black, red, and blue lines

coefficients of determination (R^2). According to Fig. 5h, the largest discrepancy between the CERES observed and calculated TOA SW fluxes occur in the mid-latitudes (25–35%). By inspection of their globally distributed differences (Fig. 5e, f), the large mid-latitude differences seem to be limited to the oceans and Southeast Asia but also over South America, Central Africa, Greenland, and Antarctica in 2B-FLXHR-LIDAR.

Due to the large footprint of CERES (20 km at nadir) and a nearly nadir view (~ 1.4 km) of CloudSat and CALIPSO, it is inappropriate to assume that, based on the methods used here, single-layered ice clouds are the only type found within the CERES footprint. It is well known that low-level marine boundary layer stratocumulus clouds frequently reside in the Southern Ocean and along the western continental coasts. Contamination of highly reflective clouds far removed

from the CloudSat and CALIPSO swaths but still within the CERES footprint (and detected by MODIS) are plausibly causing some of the discrepancy in the TOA reflected SW fluxes as shown in Fig. 5e, f. In fact, the cloud optical depth is larger for the CCCM_CC pixels, especially in the midlatitudes where the zonal mean is larger by about 2, due to the utilization of MODIS radiances in their algorithm, when compared with the collocated 2C-ICE optical depths (not shown). Based on its algorithm design, 2C-ICE is missing some high-level, highly reflective thin cirrus clouds (see Berry and Mace 2014).

Global and zonal mean comparisons of the TOA outgoing LW flux are more closely constrained than their SW counterparts. The calculated global mean TOA LW fluxes from 2B-FLXHR-LIDAR and D18 (Fig. 6a, e; b, f, respectively) are within 2% of the mean from CERES (Fig. 6d)

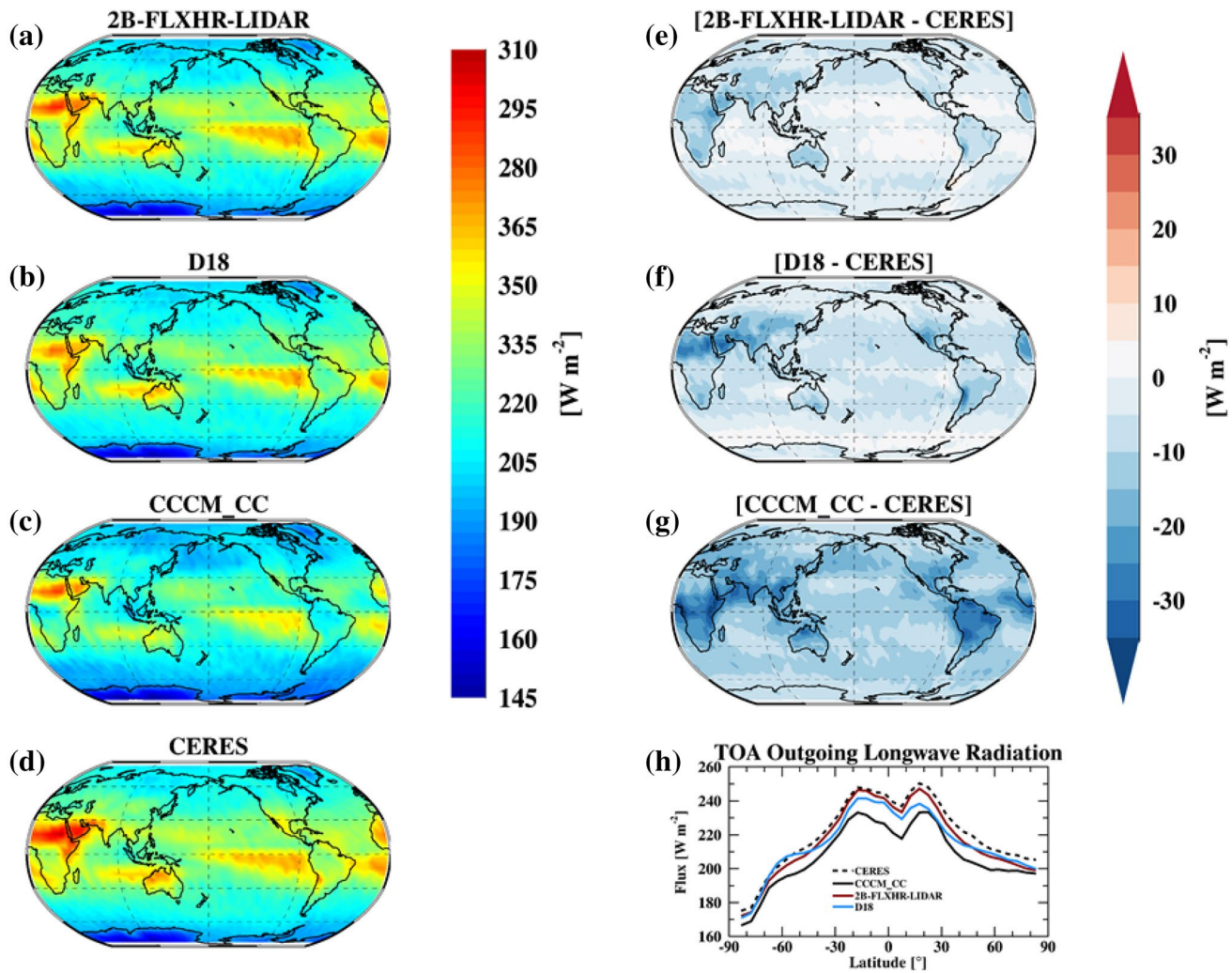


Fig. 6 Same as Fig. 5 but for the TOA outgoing LW fluxes

Table 2 Four year (2007–2010) weighted global means of the globally gridded ($5^\circ \times 5^\circ$) instantaneous daytime TOA fluxes for single-layer ice clouds calculated by D18, 2B-FLXHR-LIDAR, and CCCM_CC, as well as, the observed fluxes from CERES.

	D18				2B-FLXHR-LIDAR				CCCM_CC				CERES
	Mean	RMSD	R^2	Slope	Mean	RMSD	R^2	Slope	Mean	RMSD	R^2	Slope	Mean
Shortwave	210.19	44.64	0.59	0.85	194.45	56.12	0.64	0.83	242.20	12.18	0.92	0.95	241.52
Longwave	222.27	7.58	0.96	0.88	224.98	5.64	0.97	0.98	214.57	14.13	0.95	0.86	228.73

Root mean squared differences (RMSD) in W m^{-2} , R^2 , and slopes of the linear regression between the calculated fluxes and CERES

with RMSDs less than 8.0 W m^{-2} and correlation coefficients (R^2) of ~ 0.96 . While CCCM_CC has an even larger, albeit still relatively small, bias (RMSD = 14.13 W m^{-2}), it can be easily explained. Due to an enhanced cloud masking algorithm in CCCM_CC, cloud-top heights (and consequently their infrared emission temperature) are better retrieved and ultimately used in their computations (Kato et al. 2011). Therefore, CERES and CCCM_CC provide

the upper and lower bounds of the observed TOA outgoing LW flux.

Passive sensors (i.e., MODIS) operate at an inherent disadvantage in detecting optically thin, relatively cold-topped clouds (Ackerman et al. 2008; Holz 2016; Marquis et al. 2017). As a result, any algorithm using only passive cloud retrievals to study the effects of ice clouds on the TOA radiation may not be adequately represented, especially at the

resolution of CloudSat and CALIPSO. In the study by Kato et al. (2011), the TOA LW irradiances for 1 month of data are examined for CCCM_CC and an algorithm using only MODIS-retrieved cloud properties. They concluded that the TOA outgoing LW flux from CCCM_CC is closer to CERES than the MODIS only product due to the detection limitations of MODIS. Furthermore, the impacts of multi-layered cloud systems on the computed TOA fluxes are also investigated. In a scenario where an optically thin ice cloud overlays a liquid cloud, the difference in OLR can amount to more than 100 W m^{-2} depending on the phase, height, and optical properties of the overlapping cloud system (Kato et al. 2011; Yi et al. 2017a, b). This result also supports the point we made in the previous section about how the large CERES footprint may not well represent the CloudSat/CALIPSO swath. In this case, the proximity of lower-level liquid clouds (or the clear-sky) would increase the TOA OLR for individual pixels, and most certainly for a grid box of $5^\circ \times 5^\circ$.

Computed surface downward SW and LW fluxes are evaluated based on the observed fluxes at three Department of Energy (DOE) ARM Climate Research Facilities. Comparing the calculated surface fluxes with the observed ones adds further robustness to the calculated radiative flux profiles investigated further below. If the TOA and surface fluxes agree well with observations, we will have higher confidence in the calculated fluxes within the atmosphere and, more importantly for the cloud heating rate profiles. The observed 10-min average surface radiative fluxes come from upward and downward facing Eppley precision spectral pyranometers and infrared pyrgeometers. The estimated uncertainties of downward SW and LW fluxes are ± 10 and 4 W m^{-2} , respectively (Long and Shi 2008). The calculated instantaneous fluxes are selected for each ARM site assuming they are within a 120 km^2 box centered at the site.

The Southern Great Plains (SGP; $36^\circ 36' 18''\text{N}$, $97^\circ 29' 6''\text{W}$) site has the fewest number of collocated cases with 19, all of which occur during the nighttime. As a result, only the LW fluxes are analyzed. Based on the scatterplot in Fig. 7b, all three data sets show skill in calculating the surface downward LW flux. In fact, their sample means are all within 1% of the ARM mean and with similar standard deviations (i.e., Table 3).

The Tropical Western Pacific (TWP; $0^\circ 31' 15.6''$, $166^\circ 54' 57.6''\text{E}$) site located on Nauru (-C2) Island yielded 32 cases, all of which occur during the day due to the A-Train overpass configuration (1:30 pm equator transect). Scatterplots of the downward SW flux (Fig. 7c) suggest some persistent errors in the calculated fluxes. On average, the calculated fluxes from D18, 2B-FLXHR-LIDAR, and CCCM_CC are 15%, 17%, and 9%, respectively, greater than the ARM observations (although with very large RMSDs), and their standard deviations are much too small (see

Table 3). When the ARM-observed downward SW fluxes are less than $\sim 500 \text{ W m}^{-2}$, the corresponding calculated pixels are significantly too high (by up to 700 W m^{-2}). The large standard deviation in the downward SW flux in the ARM data also suggests a wide range of cloud optical properties ($2\text{C-ICE IWP} = 0.05\text{--}225 \text{ g m}^{-2}$, although 75% of these IWPs are below 5.0 g m^{-2}). The calculated downward LW fluxes match better with the ARM observed fluxes at TWP-C2; fractional differences are less than 4%.

Finally, a total of 30 cases (20 daytime, 10 nighttime) were collocated with the North Slope of Alaska (NSA; $71^\circ 19' 22.8''\text{N}$, $156^\circ 36' 32.4''\text{W}$) site in Barrow, Alaska. The scatterplot in Fig. 7e suggests that the calculated fluxes during high SZAs or for optically thick single-layered ice clouds, and hence a small surface SW transmission, are well matched with ARM observations. However, when the downward SW flux from ARM is larger, there is a larger discrepancy. On average, the calculated surface downward SW fluxes from D18 and 2B-FLXHR-LIDAR are more than 50 W m^{-2} ($\sim 20\%$) greater than the ARM data. The cause of this discrepancy is plausibly due to an improper representation of cloud optical (i.e., too thin or particle size too large) or aerosol properties. However, assumptions related to ice particle habit and ice particle size distribution in the respective RTMs could also contribute to the bias. The calculated surface downward LW fluxes are underestimated by ~ 30 (12%) and ~ 16 (5%) W m^{-2} by D18 and 2B-FLXHR-LIDAR, respectively, with no discernable difference in modeled errors between day and night.

4.2 Cloud radiative heating rate profiles

The radiative heating rate (Q_r) is a concept of flux divergence with positive (negative) values representing heating (cooling) within a layer. For this study, radiative heating rate profiles are determined from the calculated flux profiles as:

$$Q_r(\text{K day}^{-1}) = \frac{\partial T}{\partial t} = -\frac{1}{\rho c_p} \frac{dF_{net}}{dz} = \frac{g}{c_p} \frac{dF_{net}}{dp}, \quad (1)$$

where

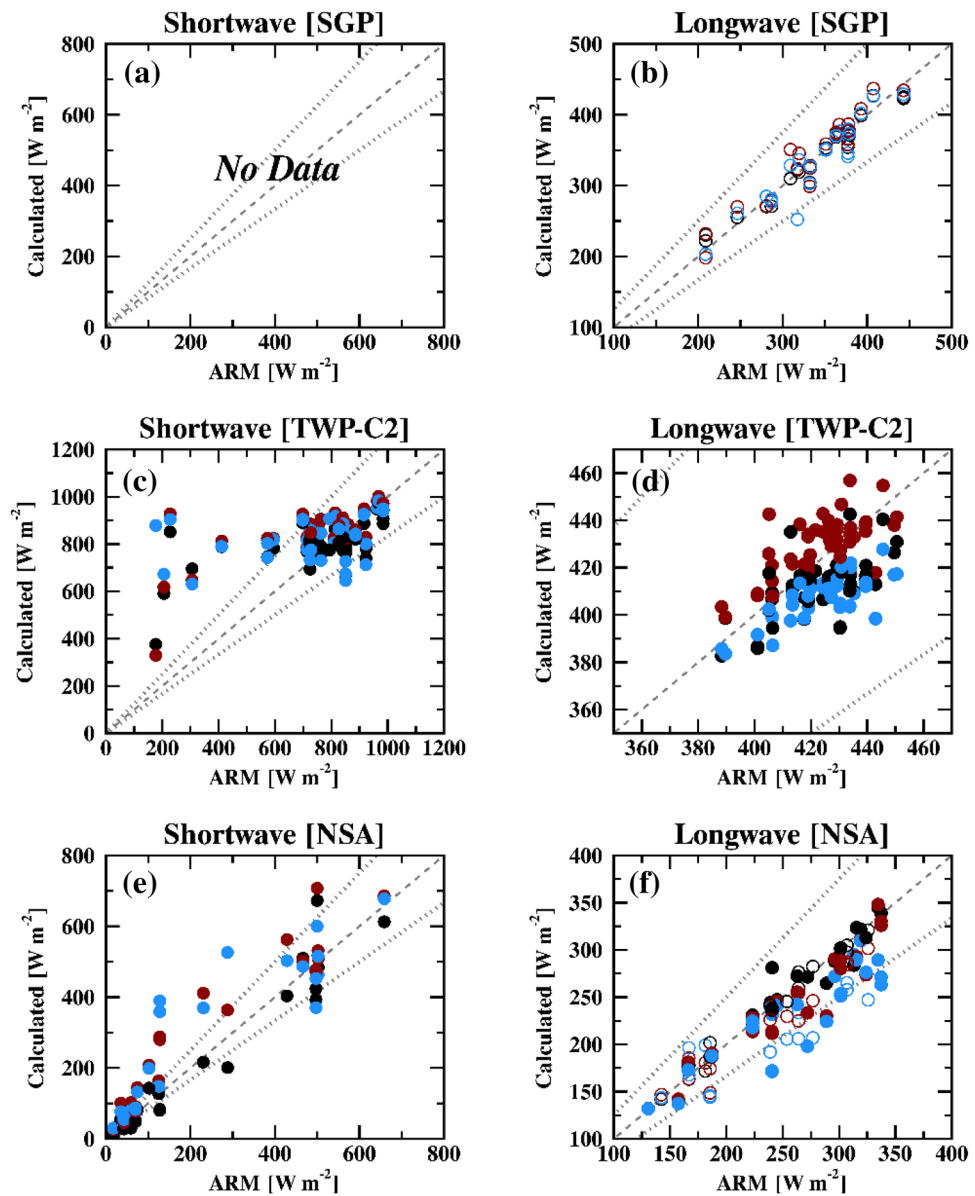
$$\Delta F_{net} = F_{net}(z + \Delta z) - F_{net}(z), \quad (2a)$$

and

$$F_{net}(z) = F^\uparrow(z) - F^\downarrow(z) \quad (2b)$$

c_p is the specific heat at constant pressure ($1004 \text{ J kg}^{-1} \text{ K}^{-1}$), ρ is the density of dry air (1.225 kg m^{-3} at standard temperature and pressure), and g is the gravitational constant (9.80665 m s^{-1}). While 2B-FLXHR-LIDAR provides estimates of heating rate profiles, we use the upward and downward radiative flux profiles to calculate the radiative heating rate profiles of single-layered ice clouds based on

Fig. 7 Scatterplots of the calculated downward SW (left) and LW (right) fluxes at the ARM Southern Great Plains (SGP; top), Tropical Western Pacific, Nauru (TWP-C2, middle), and North Slope of Alaska (NSA, bottom) sites. Black, red, and blue symbols correspond to the instantaneous fluxes calculated by CCCM_CC, 2B-FLXHR-LIDAR, and D18, respectively. Open and filled symbols represent fluxes calculated and observed during the nighttime and daytime, respectively. Calculated fluxes are selected when pixels are within 20 km of the ARM site. Each point represents a pixel collocated to ARM. Grey dotted lines represent a $\pm 20\%$ bound to the ARM observed fluxes



Eq. (1) to remain consistent with the other two data sets. The heating rate profiles presented in this study are of the entire atmospheric column (i.e., containing single-layered ice clouds and the clear-sky parts above and below the cloud layer). The SW and LW radiative heating rate uncertainties are estimated to be $\sim 10\%$ and 25% , respectively, for D18 assuming an uncertainty of 15% in the 2C-ICE R_e retrieval.

To demonstrate the changes in SW heating and LW cooling produced by the presence of singled-layer ice clouds, refer to Fig. 8. The pixel-level retrieved IWC and R_e profiles from 2C-ICE, and their corresponding heating rate profiles (black line), are provided at a vertical resolution of 250 m. As previously mentioned, the 2C-ICE retrieved IWC and R_e are used in the RTM to calculate the radiative heating rate profiles. The positive heating rates (i.e., warming) indicate

net energy into the sublayer. On the other hand, negative heating rates indicate net energy away from the sublayer, and result in cooling. The large positive SW heating rates within the cloud layer are plausible due to the absorption by cloud particles, while the slight positive SW heating rates above and below the cloud layer are caused by aerosol and greenhouse gas (e.g., water vapor) absorption. The positive LW heating rates near the cloud-base are the result of absorption of LW radiation emitted from the surface, while the negative LW heating rates near the cloud-top are due to the relatively cold atmospheric temperature above the cloud layer.

To demonstrate the difference between the cloud-induced and clear-sky heating rates, the clear-sky heating rates are also produced in Fig. 8 (pink line). The calculated SW heating and LW cooling rates above the cloud layer (black lines)

Table 3 The average surface downward SW and LW fluxes calculated by D18, 2B-FLXHR-LIDAR, and CCCM_CC, as well as, the observed fluxes from ground-based sensors at three ARM sites

	D18	2B-FLXHR-LIDAR	CCCM_CC	ARM
Shortwave				
SGP	–	–	–	–
TWP-C2	834.12 (84.69) 230.50	848.18 (123.01) 201.50	791.07 (105.77) 183.11	722.96 (223.90)
NSA	290.79 (220.92) 94.50	299.98 (231.01) 87.17	236.03 (223.97) 53.16	240.10 (215.29)
Longwave				
SGP	336.65 (60.60) 20.60	345.10 (58.58) 18.85	338.91 (56.22) 11.88	340.39 (57.40)
TWP-C2	407.16 (10.39) 19.43	429.85 (13.39) 12.14	413.08 (13.40) 16.25	423.91 (15.69)
NSA	221.72 (49.66) 41.01	238.08 (56.77) 21.81	251.21 (61.85) 12.11	251.20 (62.30)

Values in parentheses correspond to the standard deviation of fluxes. Bold numbers are the root mean squared differences (RMSD) between the calculated and ARM observed fluxes

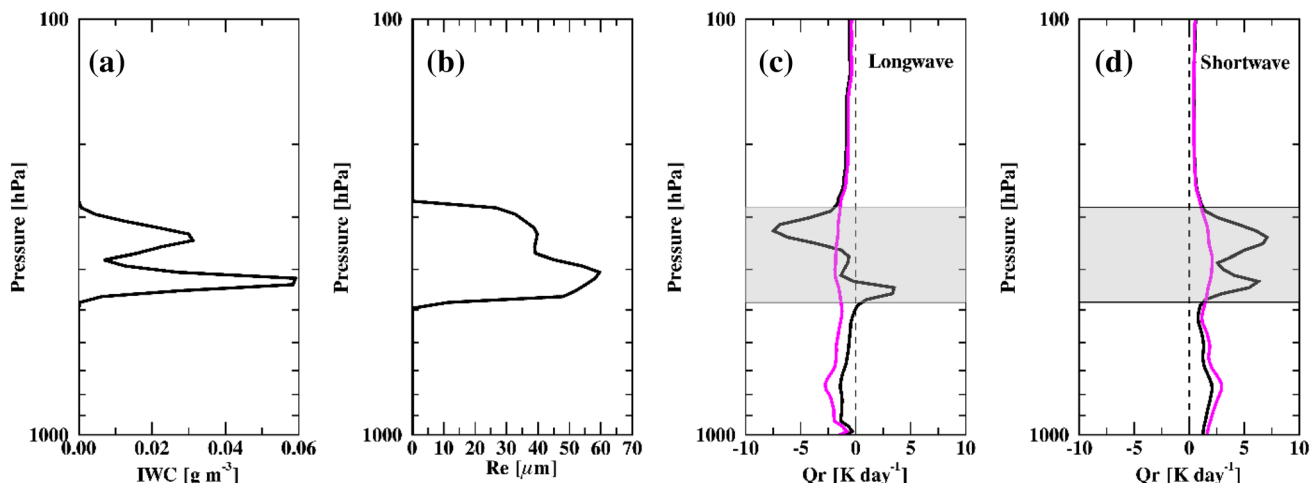


Fig. 8 The 2C-ICE retrieved vertical profiles of **a** IWC and **b** R_e , and their induced **c** LW and **d** SW heating rate profiles (black line) with the clear-sky heating rate profiles overlaid (pink) at a vertical resolu-

tion of 250 m. (Latitude = -44.3° ; longitude = 269.1° ; SZA = 36.88° ; IWP = 80.9 g m^{-2} ; $\tau = 2.8$; cloud-top height (CTH) = 9.5 km; cloud-base height (CBH) = 5.9 km; thickness = 3.6 km)

are almost identical to the clear-sky ones (pink lines). However, below the cloud layer, the magnitudes of SW heating and LW cooling rates are reduced slightly compared with the clear-sky ones, indicating that single-layered ice clouds effectively modify the atmospheric heating rates.

4.3 Zonal mean radiative heating rates profiles

The zonal mean daytime cloud radiative heating rate profiles from 2B-FLXHR-LIDAR, D18, and CCCM_CC are shown in Fig. 9. The level of zero radiative heating (i.e., $Q_r = 0 \text{ K day}^{-1}$) is highlighted with the dashed lines while the solid black lines are the zonal mean cloud boundaries determined by 2C-ICE. The strongest SW heating rates occur within the cloud in the tropics and mid-latitudes in all three datasets,

where IWC and R_e are largest on average. Considerable SW warming also extends to the surface in the tropics due to the efficient transmission of solar radiation. CCCM_CC has the strongest SW heating rates within the cloud of $> 2.5 \text{ K day}^{-1}$ (Fig. 9g), whereas 2B-FLXHR-LIDAR (Fig. 9a) has the weakest (maximum SW heating is roughly $1.5\text{--}2.0 \text{ K day}^{-1}$), and the D18 heating rates fall between them. Enhanced SW warming also occurs above $\sim 100 \text{ hPa}$ in all three data sets due to ozone absorption. In general, the SW heating rate profiles from the three datasets are quite similar with slight differences in magnitude ($\sigma \sim 0.7 \text{ K day}^{-1}$).

As illustrated in Fig. 9b, e, h, the LW cooling rates ($< -2.5 \text{ K day}^{-1}$) produced by single-layered ice clouds are strongest in the tropics several hundreds of hPa below the cloud-base, while considerable LW cooling also occurs

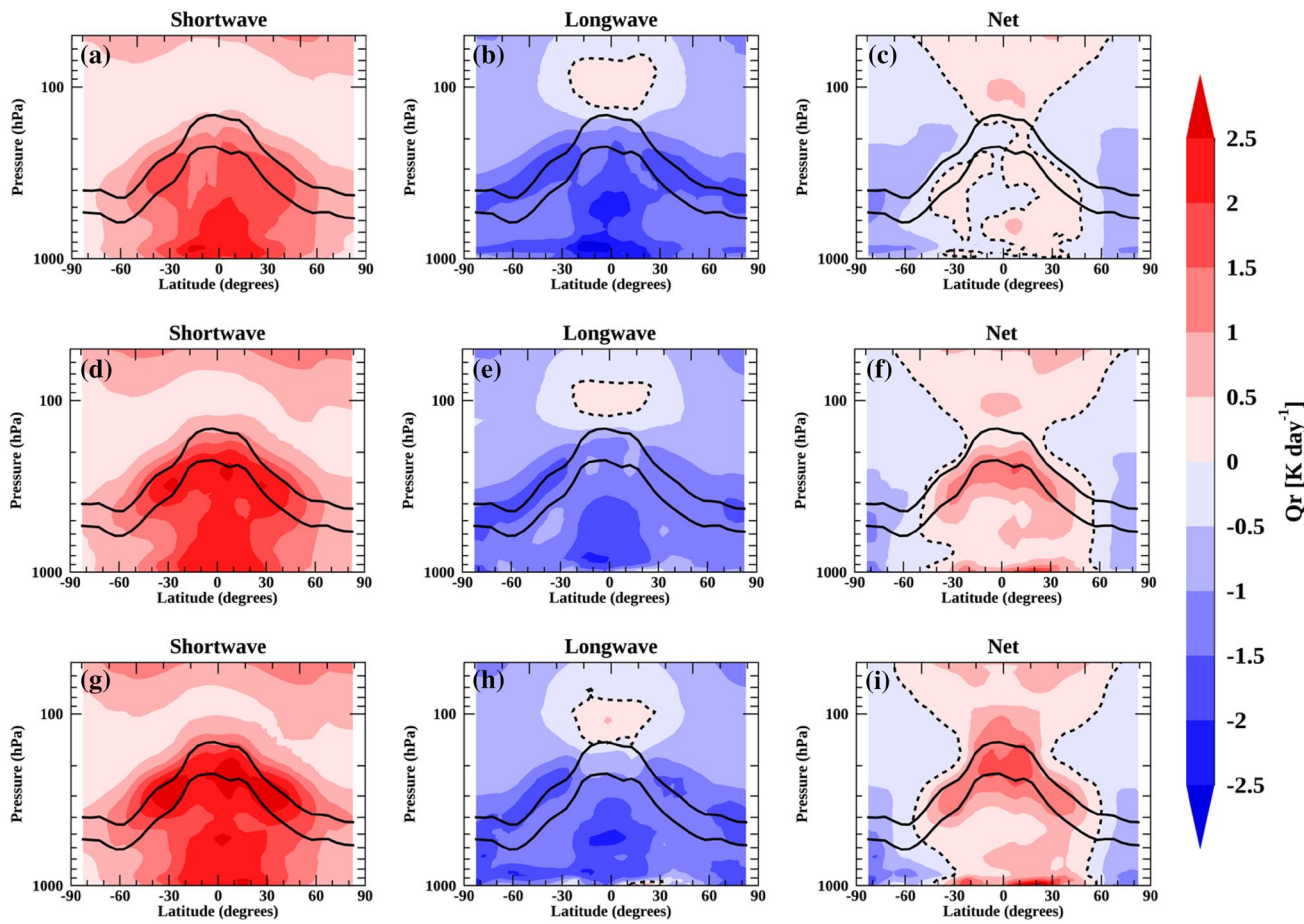


Fig. 9 The zonally averaged SW (left), LW (middle), and Net (right) daytime radiative heating rate (Q_r , $K \text{ day}^{-1}$) profiles for the selected single-layered ice clouds from (top, **a–c**) 2B-FLXHR-LIDAR, (middle, **d–f**) D18, and (bottom, **g–i**) CCCM_CC. The 0 K day^{-1} heating is highlighted with the dashed line and the solid lines represent the zonally averaged cloud-top and -base pressures

dle, **d–f**) D18, and (bottom, **g–i**) CCCM_CC. The 0 K day^{-1} heating is highlighted with the dashed line and the solid lines represent the zonally averaged cloud-top and -base pressures

at and above the cloud-top in the mid-latitudes where the largest IWCs are located. An isolated area of LW warming ($< \sim 0.5 \text{ K day}^{-1}$) is produced at $\sim 100 \text{ hPa}$ in the tropics, likely due to the large occurrence of optically thin cirrus clouds in this region. Compared with the other two datasets, D18 is unique in that it does not produce the enhanced low-level cooling features in the southern hemisphere mid- and high-latitudes. Low-level ($P > \sim 800 \text{ hPa}$) LW cooling (up to -2.0 K day^{-1} here) is indicative of boundary layer clouds (Mather et al. 2007), which were filtered out of the 2C-ICE subset. As previously noted, clouds below 1 km that go undetected by CloudSat and CALIPSO can cause the low-level cooling in 2B-FLXHR-LIDAR and CCCM_CC. This cooling feature is not surprising given that the 2B-FLXHR-LIDAR and CCCM_CC cloud properties used in calculating the fluxes profiles (see Table 1) are constrained by MODIS reflectances.

Based on the net zonal heating rate profiles in Fig. 9c, f, i, we can draw the following conclusions: the single-layered ice clouds over the tropics are the most efficient at warming

the upper troposphere ($\sim 200\text{--}300 \text{ hPa}$) and net cloud radiative cooling occurs in the high-latitudes when the instantaneous SZAs are larger (which is a byproduct of the orbit of the A-Train), and the cloud-base heights (temperatures) are lower (warmer). The patterns of net radiative heating rate profiles are similar in D18 and CCCM_CC, however, 2B-FLXHR-LIDAR is unique in that it produces negative heating rates below 200 hPa in most of the tropics caused by the relatively weak SW warming and strong LW cooling rates there. The relatively strong tropical heating rates support the deepening and stabilization of the troposphere which can in turn act to modify large scale-circulation patterns such as the Madden-Julian Oscillation (Crueger and Stevens 2015) and shift the ITCZ (Harrop and Hartmann 2016).

4.4 Composite ice water path (IWP) heating rate profiles

Changes in the cloud radiative heating rate profiles as determined by their IWP are presented in Fig. 10. On

average, the single-layered ice cloud thicknesses range from ~ 10 to 420 hPa from the smallest to largest IWPs (black lines in Fig. 10). Cloud-top and -base pressures increase from $0.1 < \text{IWP} < 5.0 \text{ g m}^{-2}$, while the clouds deepen for $\text{IWP} > \sim 50 \text{ g m}^{-2}$. Typically, the magnitude of the SW/LW/net radiative heating rates near cloud-top are primarily determined by cloud geometric and/or optical thickness (Ackerman et al. 1988); the SW heating and LW cooling rates increase with increased cloud IWP and cloud thickness as demonstrated in Fig. 10. The relatively strong SW heating rates near the cloud-top (due to more absorption of SW radiation) overwhelm the relatively strong LW cooling rates (due to the much colder atmospheric temperature above the cloud-top) effectively inducing net heating rates of more than $+5.0 \text{ K day}^{-1}$ for the thickest of single-layered ice clouds ($\text{IWP} > 5000 \text{ g m}^{-2}$, PDF $< 0.001\%$ in Fig. 3d). It is also worth noting the $\sim 5 \text{ K day}^{-1}$ variation in the net heating rates at these large IWPs between the three products (not shown). For the thinnest clouds ($\text{IWP} < 10 \text{ g m}^{-2}$), which are

most frequent, LW cooling slightly overwhelms SW heating (see Fig. 10c, f, i).

On average, for $\text{IWP} > 100 \text{ g m}^{-2}$, the strongest SW heating rates are located at the cloud-top where most of the SW absorption occurs, and then decrease toward the cloud center. Near the cloud-base, the SW heating rates are weaker due to the reduction of solar photon penetration. A region of relatively strong SW heating (up to 3.0 K day^{-1}) is produced below ~ 500 hPa for $\text{IWP} < 1.0 \text{ g m}^{-2}$ (not clear with the current contouring) whereas the in-cloud SW warming is $< 1.0 \text{ K day}^{-1}$. The enhanced SW heating in the low-levels for small IWPs are likely caused by water vapor absorption.

According to the D18 heating rate profiles, a dipole of cloud-top LW cooling and cloud-base LW warming occurs for ice clouds with $\text{IWP} > \sim 600 \text{ g m}^{-2}$. Otherwise the cloud is primarily losing heat/energy through its depth. It is common for ice clouds to induce positive LW heating rates at the cloud-base since the cloud absorbs more surface LW emission than it emits. For the same large IWPs, the

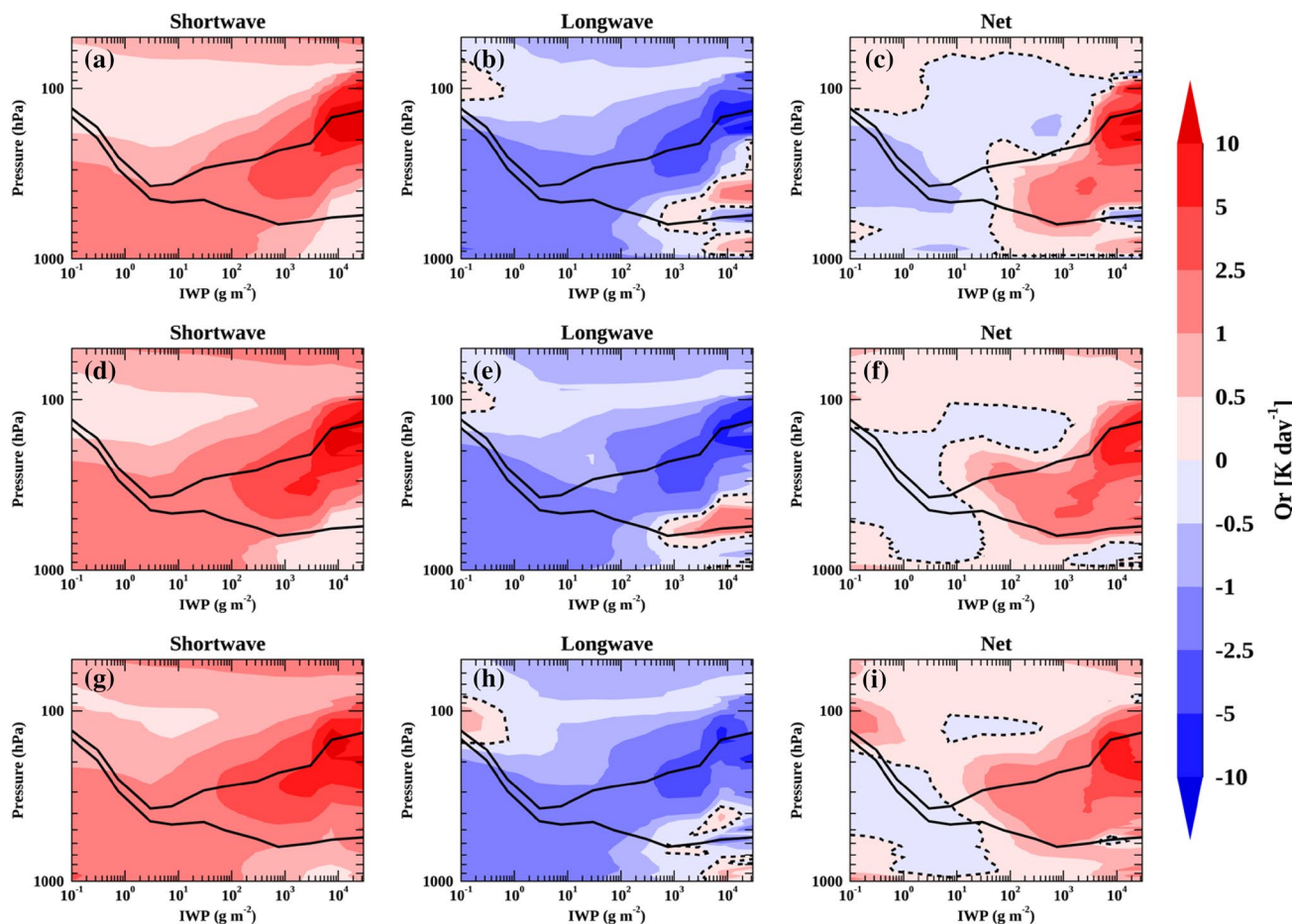


Fig. 10 Global composites of the SW (left), LW (middle), and net (right) daytime radiative heating rate (Q_r , K day^{-1}) profiles for the selected single-layered ice clouds with respect to the 2C-ICE ice water path (IWP , g m^{-2}) for 2B-FLXHR-LIDAR (top, a–c), D18

(middle, d–f), and CCCM_CC (bottom, g–i). Black lines correspond to the average cloud-top and -base pressures. There are seven IWP bins from 0.001 to $10,000 \text{ g m}^{-2}$, each increasing by an order of magnitude

2B-FLXHR-LIDAR and CCCM_CC LW heating rates show cooling at the cloud-base, but warming just above and below the cloud-base. The difference between D18 and the other two datasets suggests a variation in vertical cloud structure or differences in parameterized ice cloud properties used in their products. The positive tropical upper level LW heating rates seen in Fig. 9 are associated with IWPs less than 1.0 g m^{-2} . The low-level LW cooling seen in Fig. 9b, h are also somewhat depicted in Fig. 9b, h (i.e., the enhanced LW cooling rates for 2B-FLXHR-LIDAR and CCCM_CC, respectively). By decomposing the heating rates based on cloud IWP, it becomes clear that these low-level LW cooling rates (up to -3.0 K day^{-1}) are produced by clouds with $\text{IWP} < 10 \text{ g m}^{-2}$ according to 2C-ICE, which account for $\sim 70\%$ of the pixels (Fig. 3d).

4.5 Total column water vapor (TCWV) analysis

Diagnosing cloud radiative heating rate profiles based on water vapor variation provides a more deterministic view

into how ice clouds can be better simulated using convective cloud parameterizations in GCMs. The radiative heating rate profiles are presented as a function of total column water vapor (TCWV) in Fig. 11. The TCWV is determined by summing ($\text{TCWV} = \sum(q_v(p) \times (-dp/g))$) the water vapor mixing ratio profile from the combined ECMWF-AUX/MLS profiles used for computing the D18 heating rate profiles.

Cloud geometric thickness is rather invariant of TCWV, despite the vertical ascent of these clouds as water vapor increases. The coupling of ascending single-layered ice clouds with increasing water vapor increases the efficiency of in-cloud SW absorption, however, LW emission remains relatively constant within and below the cloud. While the three products capture a decrease in LW cooling (up to -1.5 K day^{-1}) within the cloud at $\text{TCWV} > 60 \text{ kg m}^{-2}$, the occurrence is very small (<1%). The strongest SW warming ($> 5.0 \text{ K day}^{-1}$ in CCCM_CC) also occurs in this larger TCWV regime. All three products capture the elevated LW warming due to cirrus clouds at $\text{TCWC} > 30 \text{ kg m}^{-2}$. Considering these three products, the vertical structure and

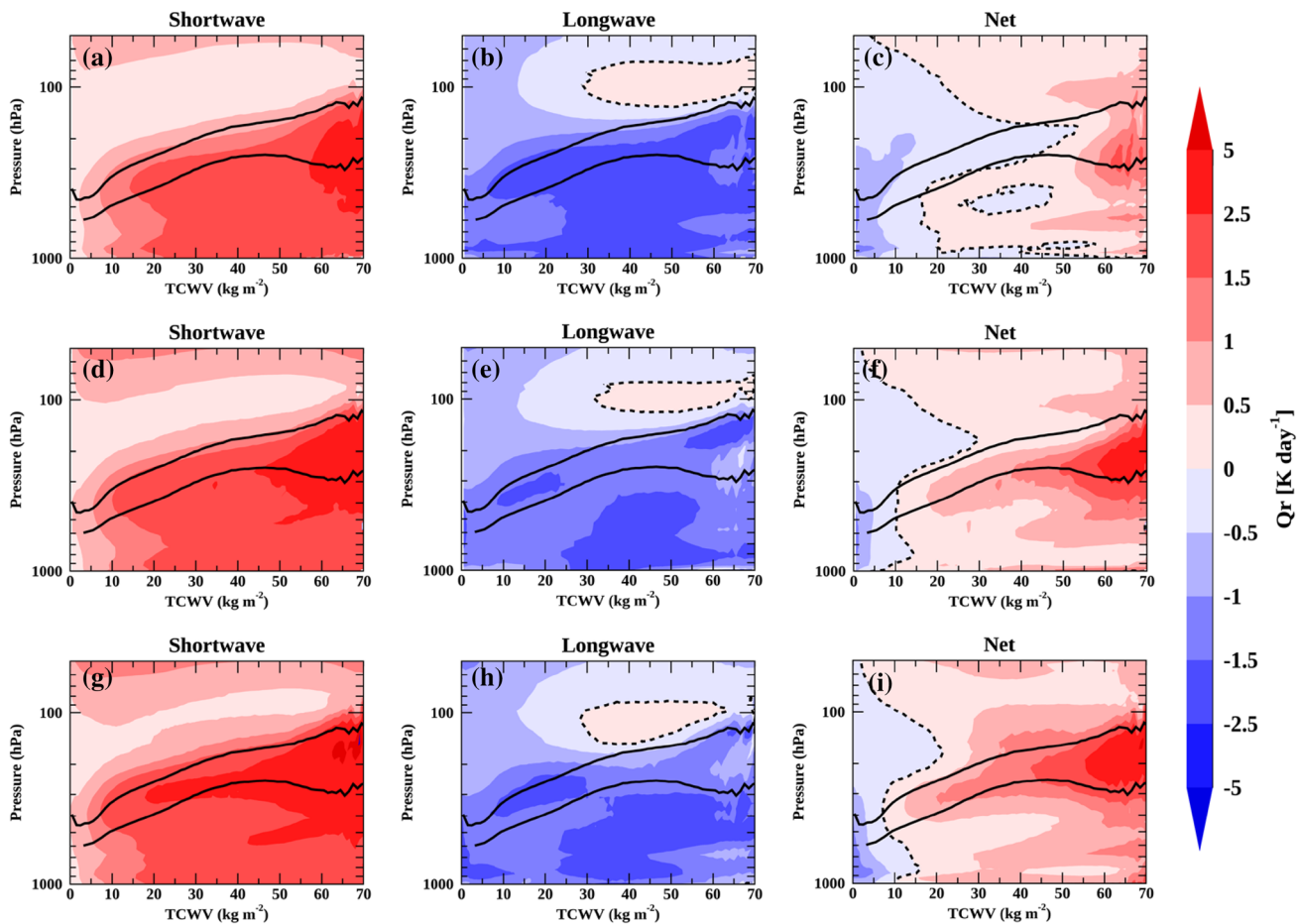


Fig. 11 Same as Fig. 10 but the heating rate profiles are a function of the total column water vapor (TCWV; kg m^{-2}) from the ECMWF/MLS profiles used in calculating the D18 fluxes

magnitude of the net radiative heating of single-layered ice clouds follows a similar structure, except at the intermediate ($25\text{--}60 \text{ kg m}^{-2}$) TCWV range.

Figure 11c, f, i show that the three products agree that there is net cooling through much of the atmosphere for $\text{TCWV} < 10 \text{ kg m}^{-2}$ (occurrence $\sim 40\%$, not shown). The above cloud net cooling extends to higher TCWV in the three products, however, 2B-FLXHR-LIDAR produces more above cloud (and even within the cloud) cooling in the intermediate TCWV range due to the stronger LW cooling there. 2B-FLXHR-LIDAR also reveals pockets of minor cooling (on the order of -0.01 K day^{-1}) below the cloud, which is not suggested by D18 or CCCM_CC. D18 and CCCM_CC consistently produce a positive gradient in the in-cloud net warming from the intermediate to high TCWV values. The vertical structure of net heating rates for $\text{TCWV} > 60 \text{ kg m}^{-2}$ are very similar among the three products, where the strongest net warming occurs within the cloud.

5 Conclusions

The active sensors on CloudSat and Cloud-Aerosol Lidar and Infrared Pathfinder Satellite (CALIPSO) provide global measurements of the vertical structure of ice clouds and have proven to be invaluable for better constraints of their radiative effects. In the present study, vertically-derived cloud properties are used to calculate the radiative heating rate profiles of single-layered ice clouds. Using the cloud properties derived from the CloudSat and CALIPSO Ice Cloud Property Product (2C-ICE), we generate an independent product of shortwave (SW) and longwave (LW) heating rate profiles and compare them to the ones from the 2B-FLXHR-LIDAR and CCCM_CC products. Based on this study, the following conclusions can be made:

1. The global occurrence frequency of non-precipitating single-layered ice clouds (with no underlying liquid clouds present) is roughly 18% with considerable occurrence ($> 25\%$) in the tropical western Pacific warm pool and central Africa above 12 km. The largest ice water path/content (IWP/C) and effective radius (R_e) are in the tropics and mid-latitudes along oceanic storm tracks. Single-layered ice clouds are relatively high in altitude and cold, as 50% of the cloud samples have cloud-top heights above 10 km and cloud-top temperatures below 215 K. Based on the probability distributions (PDFs) of cloud-top temperature (CTT), it is evident that modes of ice exist in the subset and should be uniquely handled in the radiative transfer model [i.e., cirrus (CTT $\sim 210 \text{ K}$) and glaciated ice (CTT $\sim 260 \text{ K}$)].
2. Computed top-of-atmosphere (TOA) and surface irradiances from three independent products are compared

with satellite and ground-based equivalents to assess consistency and uncertainty. We generate our own radiative flux profiles (D18) using the retrieved single-layered ice cloud microphysical properties from 2C-ICE, while 2B-FLXHR-LIDAR and CCCM_CC use retrieved cloud information from a merged CloudSat, CALIPSO, and Moderate Resolution Infrared Spectroradiometer (MODIS) product. According to their global means, the D18 and 2B-FLXHR-LIDAR TOA reflected SW fluxes for daytime single-layered ice clouds are too small by 13–20% compared to CERES and an appreciable large negative bias (25–35%) is found in the mid- and high-latitude oceans. However, the calculated TOA outgoing LW fluxes are mostly consistent (global means are within 8.0 W m^{-2}) with Clouds and the Earth Radiant Energy System (CERES) satellite observations. Instantaneous calculated surface fluxes are collocated with observed radiative fluxes at three Atmospheric Radiation Measurement (ARM) Program sites [Southern Great Plains (SGP), North Slope of Alaska (NSA), and Tropical Western Pacific (TWP)—Nauru (C2)]. Computed surface downward LW fluxes at the three ARM sites are generally well matched with the observed fluxes given the relatively small sample size (81 total). Surface downward SW fluxes, on the other hand, show a considerable positive bias [e.g., > 100 (50) W m^{-2} for D18 at TWP-C2 (NSA)].

3. Daytime cloud radiative heating rate profiles are calculated using the 2C-ICE ice cloud retrievals of IWC and R_e . Based on their zonal means, the strongest SW heating rates occur within the cloud in the tropics and mid-latitudes in all three data sets where IWC and R_e are largest on average. However, considerable SW warming also extends to the surface in the tropics. Relatively strong LW cooling rates also occur in the tropics below the single-layered ice cloud and mid-latitudes just above the cloud. In general, the patterns of SW heating and LW cooling rate profiles from three datasets are quite similar to each other with slight differences in magnitude. High-latitude net radiative cooling is determined due to the lower/warmer cloud-bases and small IWP. 2B-FLXHR-LIDAR is unique in that it produces much weaker net warming and/or net cooling rates in the tropics.
4. Daytime cloud radiative heating rate profiles are composited based on the 2C-ICE IWP and ECMWF-AUX/MLS total column water vapor (TCWV). Sorting the heating rate profiles in this way provides more detail about how heating rates vary based on retrieved cloud and environmental properties, but can also serve as a diagnostic tool used for evaluating and improving convective parameterizations. Cloud-top SW (LW) warming (cooling) is coupled with cloud-base LW warming for the largest IWPs ($> 300 \text{ g m}^{-2}$). In general, the mag-

nitudes of SW/LW/net radiative heating rates near the cloud-top are primarily determined by cloud geometric and/or optical thickness (i.e., IWP), as the SW heating and LW cooling rates increase with increased cloud IWP and cloud thickness. Considerable net cloud warming is determined for the largest IWPs and TCWV within the cloud. An upper level LW warming feature is consistently produced for tropical cirrus clouds where IWPs are smaller ($< 1.0 \text{ g m}^{-2}$) and TCWV is larger ($> 30 \text{ kg m}^{-2}$).

The present study provides useful metrics for diagnosing errors in simulated ice clouds in the form of radiative heating rate profiles as a function of different cloud and environmental states from three independently produced products. The discrepancies of TOA and surface radiative fluxes and heating rate profiles of single-layered ice clouds are assumed to be the result of different radiative transfer models used (and their subsequent parameterization assumptions regarding ice particle habit and PSD), input data (which includes different methods for retrieving cloud microphysical properties), and the difference in sampling area (L'Ecuyer et al. 2015). Furthermore, the uncertainties in computed radiative flux profiles resulting in different ice models used in parameterizing cloud optical properties and in the cloud retrievals themselves should be acknowledged. Since this study does not match the parameterized ice models used in cloud retrievals and in the RTM, some large differences in the computed radiative fluxes can occur ($\sim 16 \text{ W m}^{-2}$ in the TOA SW ice CRE; Yi et al. 2017a, b).

Acknowledgements This research was primarily supported by the NASA CERES project under Grant NNX17AC52G at the University of Arizona. Ms Erica Dolinar was supported by NASA Earth and Space Science Fellowship Program (NESSF) for her PhD degree. She was also supported by the NASA ROSES-MAP program during her internship at the Jet Propulsion Laboratory and the American Society for Engineering Education (ASEE) during her post-doc. Jonathan Jiang and Hui Su acknowledge the support by the NASA ROSES CCST and MAP programs, and by Jet Propulsion Laboratory, California Institute of Technology, under contract with NASA. Norman Loeb is supported by NASA's Radiation Budget Science Project. Author JRC acknowledges the support of the Naval Research Laboratory Base Program (BE033-03-45-T008-17). We would also like to thank Dr Greg Elsaesser for his correspondence regarding the importance of ice clouds properties in the NASA GISS GCM and Dr. Min Deng for her help to explain the 2C-ICE product.

References

- Ackerman SA, Liou KN, Valero FPJ, Pfister L (1988) Heating rates in tropical anvils. *J Atmos Sci* 45:1606–1623
- Ackerman SA, Holz RE, Frey R, Eloranta EW, Maddux BC, McGill M (2008) Cloud detection with MODIS. Part II: validation. *J Atmos Ocean Technol* 25:1073–1086. <https://doi.org/10.1175/2007JTECHA1053.1>
- Austin RT, Stephens GL (2001) Retrieval of stratus cloud microphysical parameters using millimeter-wave radar and visible optical depth in preparation for CloudSat. *J Geophys Res* 106(D22):28233–28242
- Austin RT, Heymsfield AJ, Stephens GL (2009) Retrieval of ice cloud microphysical parameters using the CloudSat millimeter-wave radar and temperature. *J Geophys Res* 114(A23):D00. <https://doi.org/10.1029/2008JD010049>
- Barker HW, Stephens GL, Fu Q (1999) The sensitivity of domain-averaged solar fluxes to assumptions about cloud geometry. *Q J R Meteorol Soc* 125:2127–2152
- Berry E, Mace GG (2014) Cloud properties and radiative effects of the Asian summer monsoon derived from A-Train data. *J Geophys Res Atmos*. <https://doi.org/10.1002/2014JD021458>
- Campbell JR, Sassen K, Welton EJ (2008) Elevated cloud and aerosol layer retrievals from micropulse lidar signal profiles. *J Atmos Ocean Technol* 25:685–700. <https://doi.org/10.1175/2007JTECHA1034.1>
- Campbell JR, Vaughan MA, Oo M, Holz RE, Lewis JR, Welton EJ (2015) Distinguishing cirrus cloud presence in autonomous lidar measurements. *Atmos Meas Tech* 8:435–449. <https://doi.org/10.5194/amt-8-435-2015>
- Campbell JR, Lolli S, Lewis JR, Gu Y, Welton EJ (2016) Daytime cirrus cloud top-of-the-atmosphere radiative forcing properties at a midlatitude site and their global consequences. *J Appl Meteorol Climatol* 55:1667–1679. <https://doi.org/10.1175/JAMC-D-15-0217.1>
- Cesana G, Waliser DE, L'Ecuyer T, Jiang X, Li J-LF (2017) Evaluation of radiative heating rate profiles in eight GCMs using A-train satellite observations. *PAIP Conf Proc* 1810:070001. <https://doi.org/10.1063/1.4975522>
- Chiriaco M et al (2007) Comparison of CALIPSO-like, LaRC, and MODIS retrievals of ice-cloud properties over SIRTA in France and Florida during CRYSTAL-FACE. *J Appl Meteorol Clim* 46:249–272. <https://doi.org/10.1175/JAM2435.1>
- Crueger T, Stevens B (2015) The effect of atmospheric radiative heating by clouds on the Madden-Julian Oscillation. *J Adv Model Earth Syst* 7:854–864. <https://doi.org/10.1002/2015MS000434>
- Cziczo DJ, Froyd KD, Hoose C, Jensen EJ, Diao M, Zondlo MA, Smith JB, Twohy CH, Murphy DM (2013) Clarifying the dominant sources and mechanisms of cirrus cloud formation. *Science* 340:1320–1324. <https://doi.org/10.1126/science.1234145>
- Del Genio AD, Wu J, Chen Y (2012) Characteristics of mesoscale organization in WRF simulations of convection during TWP-ICE. *J Clim* 25:5666–5688. <https://doi.org/10.1175/JCLI-D-11-00422.1>
- Deng M, Mace GG, Wang Z, Okamoto H (2010) Tropical composition, cloud and climate coupling experiment validation for cirrus cloud profiling retrieval using CloudSat radar and CALIPSO lidar. *J Geophys Res* 115(J15):D00. <https://doi.org/10.1029/2009JD013104>
- Deng M, Mace GG, Wang Z, Berry E (2015) CloudSat 2C-ICE product update with a new Ze parameterization in lidar-only region. *J Geophys Res Atmos* 120(208):198–212. <https://doi.org/10.1002/2015JD023600>
- Elsaesser GS, Del Genio AD, Jiang J, van Lier-Walqui M (2017) An improved convective ice parameterization for the NASA GISS global climate model and impacts on cloud ice simulation. *J Clim* 30(1):317–336. <https://doi.org/10.1175/JCLI-D-16-0346.1>
- Froidevaux L et al. (2008) Validation of aura microwave limb sounder stratospheric ozone measurements. *J Geophys Res* 113:D15S20. <https://doi.org/10.1029/2007JD008771>
- Fu Q, Liou KN (1993) Parameterization of the radiative properties of cirrus clouds. *J Atmos Sci* 50:2008–2025
- Fu Q, Liou KN, Cribb M, Charlock T, Grossman A (1997) On multiple scattering in thermal infrared radiative transfer. *J Atmos Sci* 54:2799–2812, [https://doi.org/10.1175/1520-0469\(1997\)054<2799:OMSITI>2.0.CO;2](https://doi.org/10.1175/1520-0469(1997)054<2799:OMSITI>2.0.CO;2)

- [org/10.1175/1520-0469\(1997\)054%3C279%3B:MSPITI%3E2.0.CO;2](https://doi.org/10.1175/1520-0469(1997)054%3C279%3B:MSPITI%3E2.0.CO;2).
- Harrop BE, Hartmann DL (2016) The role of cloud radiative heating in determining the location of the ITCZ in aquaplanet simulations. *J Clim* 29:2741–2763. <https://doi.org/10.1175/JCLI-D-15-0521.1>
- Hartmann DL, Ockert B-ME, Michelsen ML (1992) The effect of cloud type on earth's energy balance: global analysis. *J Clim* 5:1281–1304
- Haynes JM, L'Ecuyer TS, Stephens GL, Miller SD, Mitrescu C, Wood NB, Tanelli S (2009) Rainfall retrieval over the ocean with spaceborne W-band radar. *J Geophys Res* 114:D00A22. <https://doi.org/10.1029/2008JD009973>
- Henderson DS, L'Ecuyer T, Stephens G, Partain P, Sekiguchi M (2013) A multisensor perspective on the radiative impacts of clouds and aerosols. *J Appl Meteorol Clim* 52:853–871. <https://doi.org/10.1175/JAMC-D-12-025.1>
- Hogan RJ, Illingworth AJ (2000) Deriving cloud overlap statistics from radar. *Q J R Meteorol Soc* 126:2903–2909
- Holz RE et al (2016) Resolving ice cloud optical thickness biases between CALIOP and MODIS using infrared retrievals. *Atmos Chem Phys* 16:5075–5090. <https://doi.org/10.5194/acp-16-5075-2016>
- Jiang JH et al (2010) Five-year (2004–2009) observations of upper tropospheric water vapor and cloud ice from MLS and comparisons with GEOS-5 analyses. *J Geophys Res* 115:D15103. <https://doi.org/10.1029/2009JD013256>
- Jiang JH et al (2012) Evaluation of cloud and water vapor simulations in CMIP5 climate models using NASA "A-Train" satellite observations. *J Geophys Res* 117:D14105. <https://doi.org/10.1029/2011JD017237>
- Jiang JH et al. (2015) Evaluating the diurnal cycle of upper-tropospheric ice clouds in climate models using SMILES observations. *J Atmos Sci.* <https://doi.org/10.1175/JAS-D-14-0124.1>
- Jiang JH et al. (2017) A simulation of ice cloud particle size, humidity and temperature measurements from the TWICE CubeSat. *Earth Sp Sci*
- Kahn BH, Takahashi H, Stephens GL, Yue Q, Delanoë J, Manipon G, Manning EM, Heymsfield AJ (2018) Ice cloud microphysical trends observed by the atmospheric infrared sounder. *Atmos Chem Phys* 18:10715–10739. <https://doi.org/10.5194/acp-18-10715-2018>
- Kato S, Ackerman TP, Mather JH, Clothiaux EE (1999) The k-distribution method and correlated-k approximation for a shortwave radiative transfer model. *J Quant Spectrosc Radiat Transf* 62:109–121. [https://doi.org/10.1016/S0022-4073\(98\)00075-2](https://doi.org/10.1016/S0022-4073(98)00075-2)
- Kato S, Rose FG, Charlock TP (2005) Computation of domain-averaged irradiance using satellite derived cloud properties. *J Atmos Oceanic Technol* 22:146–164. <https://doi.org/10.1175/JTECH-1694.1>
- Kato S, Sun-Mack S, Miller WF, Rose FG, Chen Y, Minnis P, Wielicki BA (2010) Relationships among cloud occurrence frequency, overlap, and effective thickness derived from CALIPSO and CloudSat merged cloud vertical profiles. *J Geophys Res* 115:D00H28. <https://doi.org/10.1029/2009JD012277>
- Kato S et al (2011) Improvements of top-of-atmosphere and surface irradiance computations with CALIPSO-, CloudSat-, and MODIS-derived cloud and aerosol properties. *J Geophys Res* 116:D19209. <https://doi.org/10.1029/2011JD016050>
- Kato S, Miller WF, Sun-Mack S, Rose FG, Chen Y, Mlynczak PE (2014) Variable descriptions of the A-Train integrated CALIPSO, CloudSat, CERES, and MODIS merged product (CCCM or C3M), NEWS A-Train variable descriptions
- Kato SNG, Loeb DA, Rutan, Rose FG (2015) Clouds and the earth's radiant energy system (CERES) data products for climate research. *J Meteorol Soc Jpn* 93:597–612. <https://doi.org/10.2151/jmsj.2015-048>
- Kox S, Bugliaro L, Ostler A (2014) Retrieval of cirrus cloud optical thickness and top altitude from geostationary remote sensing. *Atmos Meas Tech* 7:3233–3246. <https://doi.org/10.5194/amt-7-3233-2014>
- L'Ecuyer TS, Jiang JH (2010) Touring the atmosphere aboard the A-Train. *Phys Today* 63(7):36–41. <https://doi.org/10.1063/1.3463626>
- L'Ecuyer TS, Wood NB, Haladay T, Stephens GL, Stackhouse PW Jr (2008) Impact of clouds on atmospheric heating based on the R04 CloudSat fluxes and heating rates data set. *J Geophys Res* 113:D00A15. <https://doi.org/10.1029/2008JD009951>
- L'Ecuyer TS et al (2015) The observed state of the energy budget in the early twenty-first century. *J Clim* 28:8319–8346. <https://doi.org/10.1175/JCLI-D-14-00556.1>
- Larson K, Hartmann DL (2003) Interactions among cloud, water vapor, radiation, and large-scale circulation in the tropical climate. Part I: sensitivity to uniform sea surface temperature changes. *J Clim* 16:1425–1440
- Li J, Yi Y, Minnis P, Huang J, Yan H, Ma Y, Wang W, Ayers JK (2011) Radiative effect differences between multi-layered and single-layer clouds derived from CERES, CALIPSO, and CloudSat data. *J Quant Spectr Rad Trans* 112:361–375
- Li J-LF et al (2012) An observationally based evaluation of cloud ice water in CMIP3 and CMIP5 GCMs and contemporary reanalyses using contemporary satellite data. *J Geophys Res* 117:D16105. <https://doi.org/10.1029/2012JD017640>
- Liang XZ, Wang WC (1997) Cloud overlap effects on general circulation model climate simulations. *J Geophys Res* 102:11039–11047
- Loeb NG, Kato S, Loukachevitch K, Manalo-Smith N (2005) Angular distribution models for top-of-atmosphere radiative flux estimation from the clouds and the earth's radiant energy system instrument on the terra satellite. Part I: methodology. *J Atmos Ocean Technol* 22:338–351. <https://doi.org/10.1175/JTECH-1712.1>
- Loeb NG, Wielicki BA, Rose FG, Doelling DR (2007) Variability in global top-of-atmosphere shortwave radiation between 2000 and 2005. *Geophys Res Lett* 34:L03704. <https://doi.org/10.1029/2006GL028196>
- Loeb NG, Yang P, Rose FG, Hong G, Sun-Mack S, Minnis P, Kato S, Ham S, Smith WL, Hioki S, Tang G (2018) Impact of ice cloud microphysics on satellite cloud retrievals and broadband flux radiative transfer model calculations. *J Clim* 31:1851–1864. <https://doi.org/10.1175/JCLI-D-17-0426.1>
- Long CN, Shi Y (2008) An automated quality assessment and control algorithm for surface radiation measurements. *J Open Atmos Sci* 2:23–37
- Mace GG, Zhang Q, Vaughan M, Marchand R, Stephens G, Trepte C, Winker D (2009) A description of hydrometeor layer occurrence statistics derived from the first year of merged Cloudsat and CALIPSO data. *J Geophys Res* 114:D00A26. <https://doi.org/10.1029/2007JD009755>
- Marquis JW, Bogdanoff AS, Campbell JR, Cummings JA, Westphal DL, Smith NJ, Zhang J (2017) Estimating infrared radiometric satellite sea surface temperature retrieval cold biases in the tropics due to unscreened optically thin cirrus clouds. *J Atmos Ocean Technol* 34:355–373. <https://doi.org/10.1175/JTECH-D-15-0226.1>
- Mather JH, McFarlane SA, Miller MA, Johnson KL (2007) Cloud properties and associated radiative heating rates in the tropical western Pacific. *J Geophys Res Atmos.* <https://doi.org/10.1029/2006JD007555>
- Minnis P, Yost CR, Sun-Mack S, Chen Y (2008) Estimating the top altitude of optically thick ice clouds from thermal infrared satellite observations using CALIPSO data. *Geophys Res Lett* 35:L12801. <https://doi.org/10.1029/2008GL033947>

- Nazaryan H, McCormick MP, Menzel WP (2008) Global characterization of cirrus clouds using CALIPSO data. *J Geophys Res* 113:D16211. <https://doi.org/10.1029/2007JD009481>
- Ramanathan V, Cess RD, Harrison EF, Minnis P, Barkstrom BR, Ahmad E, Hartmann D (1989) Cloud-radiative forcing and climate: results from the earth radiation budget experiment. *Science* 243:57–63
- Randall DA, Wood RA, Bony S, Colman R, Fichefet T, Fyfe J, Kattsov V, Pitman A, Shukla J, Srinivasan J, Stouffer RJ, Sumi A, Taylor KE (2007) Climate models and their evaluation. In: Qin SD, Manning M, Chen Z, Marquis M, Averyt KB, Tignor M, Miller HL (eds) Climate change 2007: the physical science basis. Contribution of Working Group I to the Fourth Assessment Report of the Intergovernmental Panel on Climate Change [Solomon]. Cambridge University Press, Cambridge
- Read WG et al (2007) Aura microwave limb sounder upper tropospheric and lower stratospheric H₂O and relative humidity with respect to ice validation. *J Geophys Res* 112(S35):D24. <https://doi.org/10.1029/2007JD008752>
- Sassen K, Cho BS (1992) Subvisual-thin cirrus lidar dataset for satellite verification and climatological research. *J Appl Meteorol* 31:1275–1285
- Sassen K, Wang Z, Liu D (2008) Global distribution of cirrus clouds from CloudSat/Cloud-Aerosol lidar and infrared pathfinder satellite observations (CALIPSO) measurements. *J Geophys Res* 113(A12):D00. <https://doi.org/10.1029/2008JD009972>
- Schwartz MJ et al. (2008) Validation of the aura microwave limb sounder temperature and geopotential height measurements. *J Geophys Res* 113:D15S11. <https://doi.org/10.1029/2007JD008783>
- Stephens GL, Webster PJ (1981) Clouds and climate: sensitivity of simple systems. *J Atmos Sci* 38:235–247. [https://doi.org/10.1175/1520-0469\(1981\)038,0235:CACSO.2.0.CO;2](https://doi.org/10.1175/1520-0469(1981)038,0235:CACSO.2.0.CO;2)
- Stephens GL et al. (2002) The CloudSat mission and the A-Train: a new dimension of space-based observations of clouds and precipitation. *Bull Am Meteorol Soc*. <https://doi.org/10.1175/BAMS-83-12-1771>
- Stubenrauch CJ et al (2013) Assessment of global cloud datasets from satellites. *Bull Am Meteorol Soc* 94:1031–1049. <https://doi.org/10.1175/BAMS-D-12-00117.1>
- Su H, Jiang JH, Stephens GL, Vane DG, Livesey NJ (2009) Radiative effects of upper tropospheric clouds observed by Aura MLS and CloudSat. *Geophys Res Lett* 36:L09815. <https://doi.org/10.1029/2009GL037173>
- Virts KS, Wallace JM (2010) Annual, interannual, and intraseasonal variability of tropical tropopause transition layer cirrus. *J Atmos Sci* 67:3097–3112. <https://doi.org/10.1175/2010JAS3413.1>
- Wielicki BA, Barkstrom BR, Harrison EF, Lee RB III, Smith GL, Cooper JE (1996) Clouds and the earth's radiant energy system (CERES): an earth observing system. *Bull Am Meteorol Soc* 72:853–868
- Wild M, Ohmura A, Gilgen H, Rosenfeld D (2004) On the consistency of trends in radiation and temperature records and implications for the global hydrological cycle. *Geophys Res Lett* 31:L11201. <https://doi.org/10.1029/2003GL019188>
- Winker DM, Vaughan MA, Omar A, Hu Y, Powell KA, Liu Z, Hunt WH, Young SA (2009) Overview of the CALIPSO mission and CALIOP data processing algorithms. *J Atmos Ocean Technol* 26:2310–2323
- Yi B, Rapp AD, Yang P, Baum BA, King MD (2017a) A comparison of Aqua MODIS ice and liquid water cloud physical and optical properties between collection 6 and collection 5.1: pixel-to-pixel comparisons. *J Geophys Res Atmos*. <https://doi.org/10.1002/2016JD025586>
- Yi B, Rapp AD, Yang P, Baum BA, King MD (2017b) A comparison of Aqua MODIS ice and liquid water cloud physical and optical properties between collection 6 and collection 5.1: cloud radiative effects. *J Geophys Res Atmos*. <https://doi.org/10.1002/2016JD025654>
- Zhang H, Peng J, Jing X, Li JN (2013) The features of cloud overlapping in Eastern Asia and their effect on cloud radiative forcing. *Sci China Earth Sci* 56:737–747

Publisher's Note Springer Nature remains neutral with regard to jurisdictional claims in published maps and institutional affiliations.